pennsylvania
DEPARTMENT OF TRANSPORTATION

Resiliency of Prestressed Concrete Beams Exposed to Fire

FINAL REPORT (Revision 1)

June 30, 2023

By Zheda Zhu, Ph.D.
Spencer E. Quiel, Ph.D., P.E. (PI)
Clay J. Naito, Ph.D., P.E. (co-PI)

ATLSS Research Center
Lehigh University

COMMONWEALTH OF PENNSYLVANIA
DEPARTMENT OF TRANSPORTATION

CONTRACT # E04005
WORK ORDER # WO 07

1. Report No. FHWA-PA-2023-006-E04005 WO 07	**2. Government Accession No.**	**3. Recipient's Catalog No.**	
4. Title and Subtitle Resiliency of Prestressed Concrete Beams Exposed to Fire		**5. Report Date** May 19, 2023 (Revised June 30, 2023)	
		6. Performing Organization Code	
7. Author(s) Zheda Zhu, Ph.D. (postdoctoral researcher, zhz314@lehigh.edu) Spencer E. Quiel, Ph.D., P.E. (PI, seq213@lehigh.edu) Clay J. Naito, Ph.D., P.E. (co-PI, cjn3@lehigh.edu)		**8. Performing Organization Report No.**	
9. Performing Organization Name and Address ATLSS Research Center, Lehigh University 117 ATLSS Drive Bethlehem, PA 18015-4729		**10. Work Unit No. (TRAIS)**	
		11. Contract or Grant No. E04005 WO 07	
12. Sponsoring Agency Name and Address The Pennsylvania Department of Transportation Bureau of Planning and Research Commonwealth Keystone Building 400 North Street, 6th Floor Harrisburg, PA 17120-0064		**13. Type of Report and Period Covered** Final Report Period: Jan. 2022 to May 2023	
		14. Sponsoring Agency Code	
15. Supplementary Notes			
16. Abstract Numerical simulations were used to investigate the thermo-structural response of simple span prestressed bulb-T concrete bridge girders to fire hazards located underneath the bridge. The approach consists of three steps: (1) fire modeling, (2) heat transfer modeling, and (3) structural modeling. The effects of thermal concrete spalling are accounted for in all analyses via periodic concrete removal by implementing a semi-empirical thermal gradient relationship. The numerical approach is validated via case study for span 30NB of the I-85 bridge near Atlanta, GA that collapsed due to severe fire in 2017. The results of fire characterization and thermo-structural analysis for the prestressed bulb-T girder cross-section (which had harped strands) showed good agreement with the outcomes of the actual event and identified flexural runaway as the primary mode of fire-induced failure. The proposed approach was then applied to a sample bridge provided by PennDOT to evaluate the thermo-structural vulnerability of its prestressed bulb-T girders (with straight strands only). Fire durations longer than 60 minutes had greater likelihood of causing heavy damage to the girder, while flexural runaway was possible after 2.5 hours of exposure. Residual damage was assessed for fires that burned out before the onset of flexural runaway. As expected, fires located underneath the quarter span induced less residual deflection than fires under midspan. Numerical results indicated that the structural fire performance of these prestressed bulb-T girders is associated with strand patterns and section geometry, as well as the intensity and clearance to the fire. Deeper embedment of the prestressing strands within thicker sections of concrete will improve the response of these girders to fire.			
17. Key Words Prestressed concrete bulb-T bridge girders; fire hazard; I-85 Atlanta bridge fire case study; flexure failure; shear failure; fire-induced damage classification		**18. Distribution Statement** No restrictions. This document is available from the National Technical Information Service, Springfield, VA 22161	
19. Security Classif. (of this report) Unclassified	**20. Security Classif. (of this page)** Unclassified	**21. No. of Pages** 43	**22. Price**

EXECUTIVE SUMMARY

The Pennsylvania Department of Transportation (PennDOT) has commissioned the research team at Lehigh University to investigate the fire hazard posed by potential fuel sources stored underneath a prototype 90-ft overpass bridge that is supported by prestressed (PS) concrete bulb-T girders. This report evaluates the fire resistance of the bridge girder superstructure (including the contributions of the composite deck slab) – the piers will not be considered in the scope of this project but can be added during a subsequent phase at PennDOT's request. In this project, the fire will be evaluated only at locations directly underneath the bridge – other locations not directly underneath the bridge (i.e. either aside the bridge or on the bridge deck) could also be considered in subsequent phases at PennDOT's request. Fire protection or mitigation systems are also not considered in the scope of this study but could be considered in subsequent phases at PennDOT's request.

Generally, the thermo-structural analysis used in this study consists of three modeling stages:

- FIRE MODELING: Fire due to varying fuel sources is modeled as open-air with a heat release rate time history and burning duration developed from published literature on the combustion properties, flame characteristics, and smoke generation of the fuels in question. The approximate geometry of the fire (primarily the footprint and flame height) are developed using available semi-empirical calculation approaches.
- HEAT TRANSFER MODELING: The heat transfer from the fire to the underside of the bridge superstructure is calculated using a modified discretized solid flame (MDSF) approach, which was first developed by Quiel et al. [1] and improved in subsequent research [2]. The non-uniform temperature distribution throughout the cross-section of the PS concrete girder is simulated via 2D finite element (FE) analysis and accounts for thermally induced concrete spalling (using a simplified prediction approach based on recent experimental testing by the authors [3]). The realistic incorporation of spalling enables a more rapid progression of thermal penetration into the cross-section from fire exposure via the sudden elimination of concrete layers.
- STRUCTURAL MODELING: The flexural performance of the heated bridge girders is evaluated when subjected to in-situ gravity loading and fire exposure at three longitudinal locations along the span (midspan, quarter-span and near the support). A FE model composed of fiber-beam elements is analyzed to determine the capacity reduction of the PS concrete girder and the structurally critical locations. The temperature-dependent shear capacity is also calculated based on AASHTO LRFD [4] specifications.

Before conducting the analysis on the PennDOT PS prototype bridge, a case study is performed for the I-85 PS concrete bridge that collapsed in the 2017 due to exposure from severe fire underneath the bridge at low clearance [5]. That bridge utilized similar PS bulb-T girders, and the fire scenario is characterized based on the post-fire NSTB investigation report. The 3-stage modeling approach provides a close prediction of the time and mode of collapse for that event.

The 3-stage modeling approach is then used to evaluate the PennDOT prototype PS girders for resistance and resilience to several likely fire scenarios at a range of realistic clearance heights. For the first fire scenario, PennDOT had provided the project team with photos of large hay bale stacks that were stored underneath the bridge. A worst-case fire scenario characterization for the hay bale storage produced only minimal thermal impact on the PS girders, even when the fire was placed at low clearance. The fire scenarios were then focused on heat release rates (HRR) that correspond to vehicle fires per NFPA 502 [6]: 30 MW (bus), 70 MW (smaller heavy goods vehicle), and 150 MW (larger heavy goods vehicle). The base of the fire was placed at clearances of 15 ft, 30 ft, and 45ft. Each vehicle fire scenario was modeled as an equivalent gasoline pool fire with the same HRR, which is an approach commonly used to characterize vehicle fires for bridges and tunnels. To evaluate the fire resistance of the PS girder, steady state heating from each localized fire scenario was applied until flexural runaway (i.e. total loss of flexural resistance) was achieved. Resilience to each fire scenario was determined by performing iterative simulations in which the fire exposure is terminated (i.e., assuming burnout or extinguishment from firefighting) at escalating increments of 30 minutes up to the fire resistance time. The resulting damage for each length and severity of fire exposure is then categorized as a function of the maximum (during the fire) and residual (post-fire) deflections as follows (where L is the girder span length):

- **SUPERFICIAL**: Maximum residual deflection is less than *L/800* (based on the AASHTO LRFD [4] serviceability limit). The maximum deflection during the fire is less than *L/200* (i.e., 10x the critical deflection limit of *L/20* [7]). A small amount of repair may be needed, but the bridge most likely would not need to be closed beyond post-fire cleanup.

- **MODERATE**: Maximum residual deflection is less than *L/200* (i.e., 4x the AASHTO serviceability limit) and the maximum deflection during the fire is less than *L/100*. Significant amount of repair may be needed and possible replacement may be required.
- **HEAVY**: Maximum residual deflection is less than *L/100* (i.e., 8x the AASHTO serviceability limit) and the maximum deflection during the fire is less than *L/20.* Post-fire replacement will likely be required.
- **HAZARDOUS**: Maximum deflection during the fire is larger than *L/20*. Collapse is likely during or after the fire event. Replacement will be required.

The PennDOT PS girder section demonstrated greater fire resistance than the I-85 PS girder section even though they have the same span length and were evaluated using similar fire and gravity loading. The difference in performance is associated with the prestressed strand pattern and girder section geometry. Specifically, deeper embedment of the prestressing strands within larger sections of concrete will improve the response of these girder sections to fire. Generally, fire durations longer than 60 min had greater likelihood of causing heavy damage to the girder, while the hazardous damage may occur after 2.5 hrs of exposure. As expected, fire scenarios at the quarter span induced less residual deflection than fires located at midspan.

REVISION 1 (6/30/23):

A minor revision was made to the FE analysis of the PS bridge girder for the I-85 case study. Specifically, a slight correction was made to the 2D model of the girder cross-section to better reflect the dimensions shown in the shop drawings provided by the Georgia DOT. As a result, the time to failure for that analysis case increased by 14 minutes from that initially reported, and the analysis results continue to demonstrate good overall agreement with the reported observations of the actual event. Revisions to the I-85 case study analysis are highlighted in blue – all other analysis results in this report remain unchanged.

ACKNOWLEDGEMENTS

This work was sponsored by the Pennsylvania Department of Transportation (PennDOT) and the U.S. Department of Transportation Federal Highway Administration (FHWA) under Engineering and Construction Management System (ECMS) contract E04005, Work Order 07, entitled "Resiliency of PS concrete beams exposed to fire." This ECMS contract was administered by Michael Baker International, Moon Township, PA. Many thanks to Thomas Macioce (formerly of PennDOT, now retired), Timothy Carre (PennDOT), Robert Bondi (Michael Baker International), and others at PennDOT for their feedback and support throughout this project. Thanks also to Donn Digamon of the Georgia Department of Transportation (GaDOT) for providing documentation regarding the 2017 fire-induced collapse of the I-85 PS girder span in Atlanta, GA.

DISCLAIMER

TABLE OF CONTENTS

LIST OF FIGURES

LIST OF TABLES

INTRODUCTION

Fire has caused bridge failure in the US at a rate consistent with other hazards to which engineers dedicate significant amounts of time and money to mitigate. Recent surveys of bridge failures across the US [8–10] have indicated that common hazards such as flooding, collision, and overload constitute the majority of bridge failures. Fire, however, causes failure at a rate at least comparable to or exceeding those due to earthquake or construction defects, both of which are extensively addressed via design and inspection. Accidents involving heavy goods vehicles and fuel tanker trucks have typically caused most of the recent severe fire events involving bridge structures. These events include but are certainly not limited to the near-collapse of the I-65 overpass near Birmingham, AL in 2002; the total collapse of the MacArthur Maze I-80//I-580/I-880 interchange overpass in Oakland, CA in 2007; and the severe damage leading to demolition of the Route 22/322 overpass at I-81 near Harrisburg, PA in 2013. Fire hazards due to materials stored underneath bridges have also been highlighted by the total collapse of an I-85 overpass in Atlanta, GA in March 2017. High-density polyethylene (HDPE) conduit in a state-owned storage area underneath the overpass caught fire and caused the collapse of a 92-foot section of the overpass after approximately 45 minutes of fire exposure. That fire hazard resulted in the demolition of several adjacent spans due to structural damage from heat exposure and a projected $15 million in economic loss [5]. The storage of materials and the presence of vehicle traffic underneath bridges pose the most significant fire hazards to bridge infrastructure.

Historically, most bridges that have collapsed due to fire have been overpasses supported by steel plate girders, and most of the research literature on bridge fire response has focused on that structural system [1,9,11–15]. Prestressed concrete girders, particularly bulb-T cross-sections, are also widely used in highway overpass design, yet much less research has been conducted to date on their resistance (i.e. the capacity to resist collapse) and potential resilience (i.e. the mitigation of functionality loss if the bridge survives the fire through burnout) to severe fire. Experimentally, Wu et al. [16] examined the behavior of several post-tensioned concrete bridge girder sections under hydrocarbon fire exposure. A T-beam was shown to be more vulnerable than the box beam since both sides of the web are heated, which increases the temperature of the strands significantly. Spalling and cracking were observed at both the midspan and the supports. Liu et al. [17] conducted experiments on two prestressed concrete box beams from a fire-damaged bridge and concluded that the residual bearing capacity of the post-fire concrete girder largely depends on the maximum temperature the strands experienced during the fire event. Hou and Zhang [18] applied a fire-retardant coating to the surface of a prestressed concrete box girder and found that spalling and cracking of the concrete girder were significantly mitigated as a result, thus decreasing the strand temperature and minimizing the reduction in flexure capacity. Numerically, Song et al. [19] used ANSYS to perform thermo-structural analysis for a prestressed concrete box girder exposed to hydrocarbon fire and concluded the significant factors that influence the bearing capacity includes the thickness of the concrete cover, exposure time, and heating location. Kodur and Hatinger [20] evaluated the fire resistance of prestressed concrete double T-beams with SAFIR and found that performance relates to the fire scenario, load level, and failure criterion. Dwaikat and Kodur [21] developed a moment-curvature-based numerical method to predict the fire behavior of restrained RC beam accounting for spalling behavior, which is considered in their SAFIR analysis model. Wu et al. [16] also used ABAQUS to conduct numerical simulation of two bonded post-tensioned concrete T- and box beam bridges and was able to predict the temperatures of the strands and the performance of the girders. The difficulty of the numerical simulation lies in considering the negative contribution of spalling in the FE model. This effect can be significant, as spalling will expose underlying concrete reinforcement to elevated temperatures and thus increase the thermal penetration into the section. Despite this, the studies introduced above [16,18,20,21] do not account for spalling behavior in their models.

The Pennsylvania Department of Transportation (PennDOT) has commissioned the research team at Lehigh University to investigate the fire hazard posed by potential fuel sources stored underneath a prototype 90-ft overpass bridge that is supported by prestressed (PS) concrete bulb-T girders. This report evaluates the fire resistance of the bridge girder superstructure (including the contributions of the composite deck slab) – the piers will not be considered in the scope of this project but can be added during a subsequent phase at PennDOT's request. In this project, the fire will be evaluated only at locations directly underneath the bridge – other locations not directly underneath the bridge (i.e. either aside the bridge or on the bridge deck) could also be considered in subsequent phases at PennDOT's request. Fire protection or mitigation systems are also not considered in the scope of this study but could be considered in subsequent phases at PennDOT's request.

Generally, the thermal-structure analysis used in this study consists of three modeling stages:

- FIRE MODELING: Fire due to varying fuel sources is modeled as open-air with a heat release rate time history and burning duration developed from published literature on the combustion properties, flame characteristics, and smoke generation of the fuels in question. The approximate geometry of the fire (primarily the footprint and flame height) are developed using available semi-empirical calculation approaches.

- HEAT TRANSFER MODELING: The heat transfer from the fire to the underside of the bridge superstructure is calculated using a modified discretized solid flame (MDSF) approach, which was first developed by Quiel et al. [1] and improved in subsequent research [2]. The non-uniform temperature distribution throughout the cross-section of the PS concrete girder is simulated via 2D finite element (FE) analysis and accounts for thermally induced concrete spalling (using a simplified prediction approach based on recent experimental testing by the authors [3]). The realistic incorporation of spalling enables a more rapid progression of thermal penetration into the cross-section from fire exposure via the sudden elimination of concrete layers.
- STRUCTURAL MODELING: The flexural performance of the heated bridge girders is evaluated when subjected to in-situ gravity loading and fire exposure at three longitudinal locations along the span (midspan, quarter-span and near the support). A FE model composed of fiber-beam elements is analyzed to determine the capacity reduction of the PS concrete girder and the structurally critical locations. The temperature-dependent shear capacity is also calculated based on AASHTO LRFD [4] specifications.

Before conducting the analysis on the PennDOT PS prototype bridge, a case study is performed for the I-85 PS concrete bridge that collapsed in the 2017 due to exposure from severe fire underneath the bridge at low clearance [5]. That bridge utilized similar PS bulb-T girders, and the fire scenario is characterized based on the post-fire NSTB investigation report. The 3-stage modeling approach provides a good prediction of the time and mode of collapse for that event.

The 3-stage modeling approach is then used to evaluate the PennDOT prototype PS girders for resistance and resilience to several likely fire scenarios at a range of realistic clearance heights. For the first fire scenario, PennDOT had provided the project team with photos of large hay bale stacks that were stored underneath the bridge. A worst-case fire scenario characterization for the hay bale storage produced only minimal thermal impact on the PS girders, even when the fire was placed at low clearance. The fire scenarios were then focused on heat release rates (HRR) that correspond to vehicle fires per NFPA 502 [6]: 30 MW (bus), 70 MW (smaller heavy goods vehicle), and 150 MW (larger heavy goods vehicle). The base of the fire was placed at clearances of 15 ft, 30 ft, and 45ft. Each vehicle fire scenario is modeled as an equivalent gasoline pool fire with the same HRR, which is an approach commonly used to characterize vehicle fires for bridges and tunnels. To evaluate the fire resistance of the PS girder, steady state heating from each localized fire scenario was applied until flexural runaway (i.e. total loss of flexural resistance) was achieved. Resilience to each fire scenario was determined by performing iterative simulations in which the fire exposure is terminated (i.e. assuming burnout or extinguishment from firefighting) at escalating increments of 30 minutes up to the fire resistance time. The resulting damage for each length and severity of fire exposure is then categorized as a function of the maximum (during the fire) and residual (post-fire) deflections.

The report is divided into two sections. The first covers the I-85 overpass and 2017 fire event, and the results of those analyses are used to justify the aforementioned 3-stage modeling approach. The second section focuses on the expected performance of the PennDOT prototype PS girder bridge and assess the resilience of the system to severe fire events.

I-85 PS BRIDGE FIRE ANALYSIS

In March 2017, a massive fire broke out beneath the I-85 highway interchange in Atlanta, Georgia, causing span 30NB (a 92 ft long elevated span) to collapse as illustrated in Figure 1. The fire, which burned for over an hour from 6:05 am to 7:14 pm [5], was fueled by construction materials stored under the bridge, including seventy-six high-density polyethylene conduits and nine racks of fiberglass conduit. The spans adjacent to the collapsed span, two in the northbound direction and three in the southbound direction, as shown in Figure 1, were removed following the event by Georgia Department of Transportation (GDOT) due to structural damage from thermal exposure. This incident led to a $15 million replacement project [22], caused widespread traffic disruptions, and raised concerns about the safety of aging infrastructure across the United States. It also highlighted the potential fire hazard associated with storing combustible materials in close proximity to bridges and other critical infrastructure.

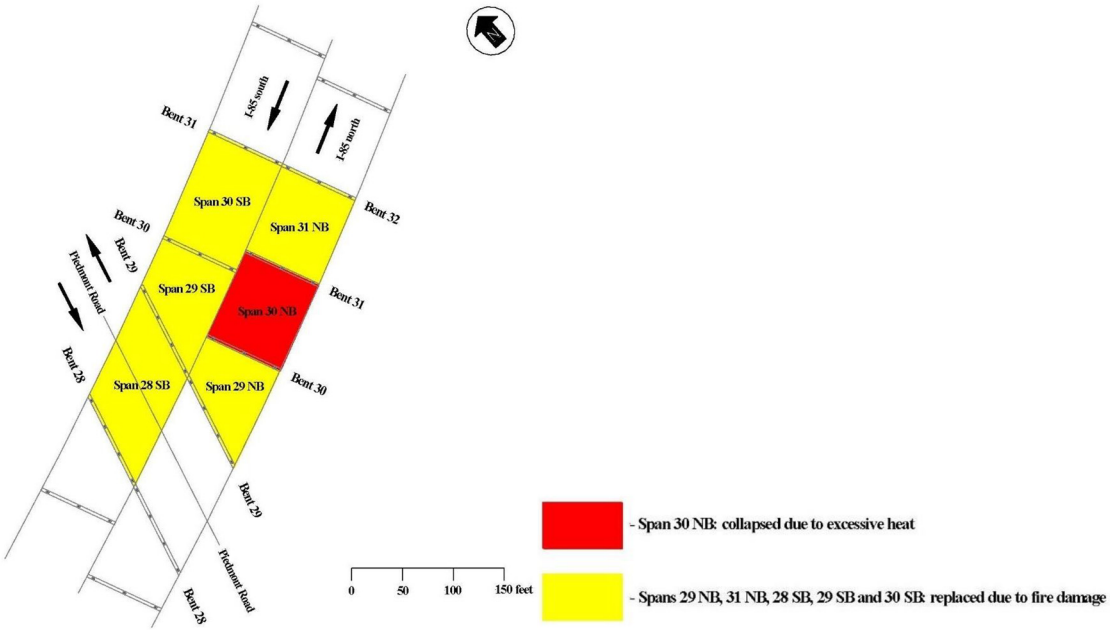

(a) Plan View [5]

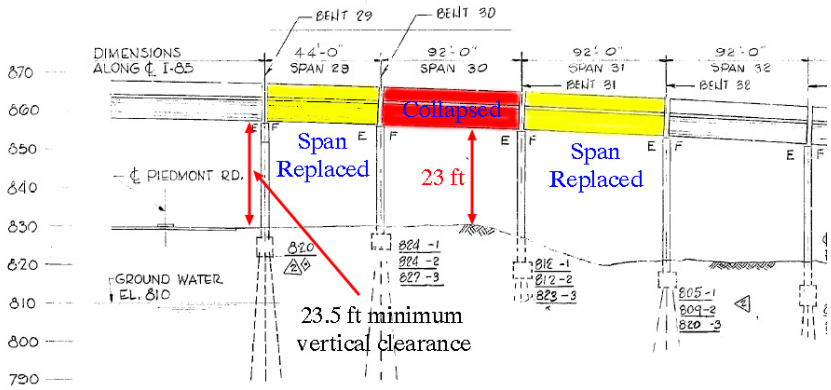

(b) Elevation View

Figure 1: Location of the collapsed span and damaged spans of the I-85 highway interchange

It was postulated in the news media that the bridge failure was attributed to weakening of the reinforcing steel and concrete during the fire hazard [23]. Detailed analysis of the event and assessment of the actual failure mode, however, was not conducted afterward. From an engineering perspective, a prestressed (PS) concrete girder is considered more fire-resistant than a similarly sized steel girder due to its larger thermal mass and lower thermal conductivity. Consequently, most bridge failures due to fire hazards have historically involved steel girder bridges (i.e., the MacArthur Maze highway interchange at Oakland, CA, that collapsed in 2007, and the Route 22/322 bridge at I-81 near Harrisburg, PA, in 2013). The failure of the PS concrete I-85 highway bridge is unusual and can serve as a case

study to help understand fire-induced failure modes in these systems and lays the groundwork for the subsequent PennDOT system analysis in this report.

Structural details

The original plan and elevation details of the collapsed span 30NB of the I-85 highway interchange, as provided by GDOT, are shown in Figure 2. The failed span measured 79 ft wide and 92 ft long from center of bent. The span was composed of nine Type V bulb-T girders spaced at 8'-10 7/8" on center. The vertical clearance from the ground to the soffit of the girders was 23 ft. The prestressed girders consist of pretensioned precast concrete GDOT Type V bulb-T girder with a height of 63 in. Two section details were provided: one detail is shown in the 1980 GDOT bridge drawing and a second 1981 "shop" detail was provided by the precast concrete producer as shown in Figure 3. Conventional precast/prestressed bridge girder design in the U.S. allows the precast producer to modify the DOT design to facilitate fabrication. The assumption is made that the 1981 shop details correspond to the as-built conditions and are therefore adopted for the thermo-structural analyses that follows.

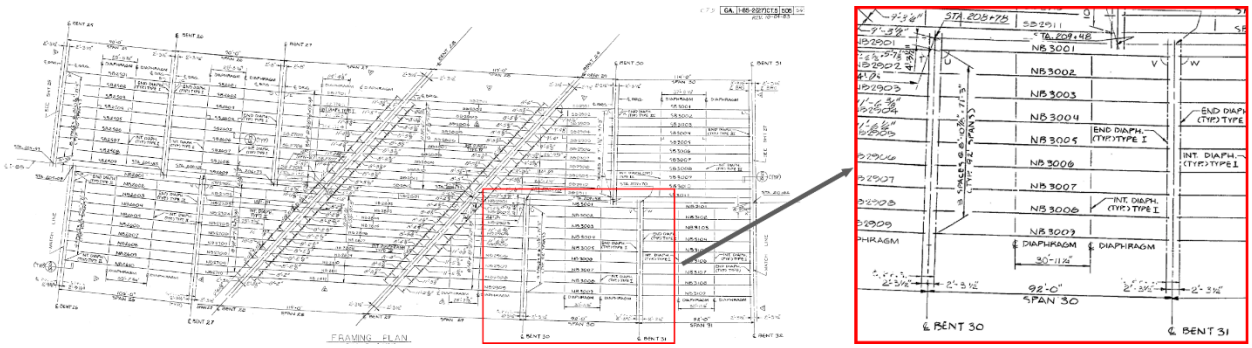

(a) Plan view and location

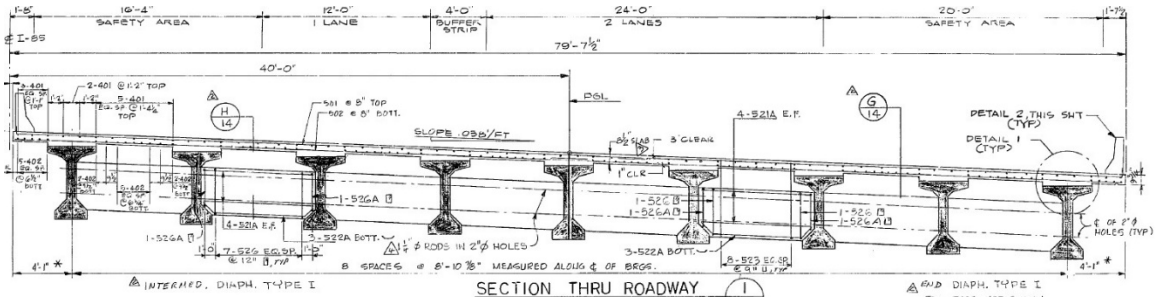

(b) Bridge section

Figure 2: Design drawings for span 30NB of I-85

Per Figure 3, the concrete girder is assumed to be prestressed with 29 ½-in. regular grade 270 7-wire strands. Five of the 29 strands are harped with a single point hold down at midspan as shown in Figure 3. The center of gravity of the strands at the midspan is 5.76 in. from the bottom of the beam at the end of the beam the center of gravity is 14.21 in. from the bottom. All strands are pre-tensioned to 28,910 lbs. Strands meet all requirements of ASTM A416 Grade 270 [24]. The mild steel reinforcement conforms to ASTM A615 Grade 60 [25]. For the prestressed concrete, the design compression strength is 5,000 psi, while the design compressive strength for the reinforced composite deck is 3,500 psi.

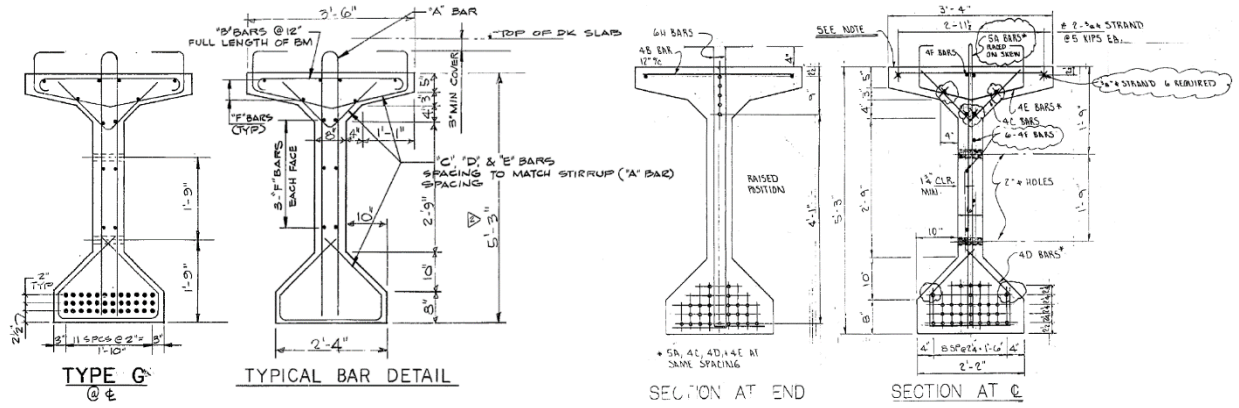

(a) Cross-section details

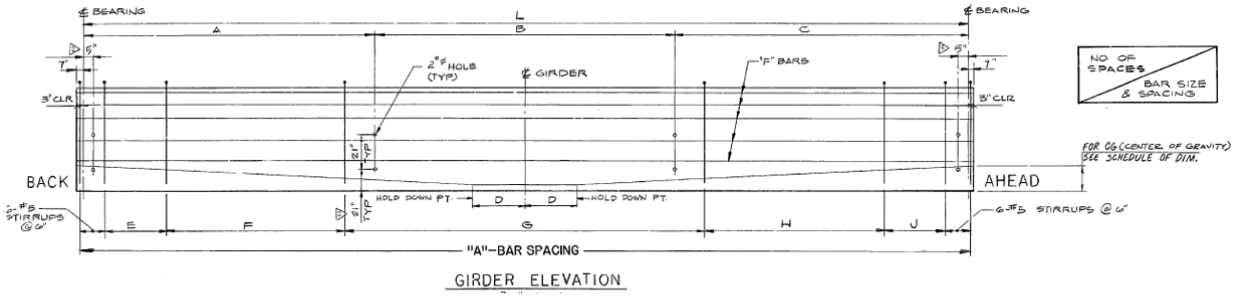

SPAN	GIRDER NO.	GIRDER TYPE	△DLNC △DLC	L	A	B	C	D	CG	E ✳	F ✳	G ✳	H ✳	J ✳
30	NB3001	G	1/16" 1/8" 1/8"	87'-6"	28'-3 3/8"	30'-11 1/4"	28'-3 3/8"	0	12.17"	7 #5@12"±	14 #5@16"±	18 #5@24"±	14 #5@16"±	7 #5@12"±
30	NB3002	G	1/16" 1/8" 1/8"	87'-8 1/8"	28'-4 1/2"	30'-11 1/4"	28'-4 3/8"	0	12.17"	7 #5@12"±	14 #5@16"±	18 #5@24"±	14 #5@16"±	7 #5@12"±
30	NB3003	G	1/16" 1/8" 1/8"	87'-10 1/4"	28'-5 1/2"	30'-11 1/4"	28'-5 1/2"	0	12.17"	7 #5@12"±	14 #5@16"±	18 #5@24"±	14 #5@16"±	7 #5@12"±
30	NB3004	G	1/16" 1/8" 1/8"	88'-0 1/2"	28'-6 5/8"	30'-11 1/4"	28'-6 3/8"	0	12.17"	7 #5@12"±	14 #5@16"±	18 #5@24"±	14 #5@16"±	7 #5@12"±
30	NB3005	G	1/16" 1/8" 1/8"	88'-2 5/8"	28'-7 5/8"	30'-11 1/4"	28'-7 3/4"	0	12.17"	7 #5@12"±	14 #5@16"±	18 #5@24"±	14 #5@16"±	7 #5@12"±
30	NB3006	△ G	1/16" 1/8" 1/8"	88'-4 3/4"	28'-8 3/4"	30'-11 1/4"	28'-8 3/4"	0	12.17"	7 #5@12"±	14 #5@16"±	18 #5@24"±	14 #5@16"±	7 #5@12"±
30	NB3007	G	1/16" 1/8" 1/8"	88'-6 7/8"	28'-9 7/8"	30'-11 1/4"	28'-9 3/4"	0	12.17"	7 #5@12"±	14 #5@16"±	18 #5@24"±	14 #5@16"±	7 #5@12"±
30	NB3008	G	1/16" 1/8" 1/8"	88'-9"	28'-10 7/8"	30'-11 1/4"	28'-10 7/8"	0	12.17"	7 #5@12"±	14 #5@16"±	18 #5@24"±	14 #5@16"±	7 #5@12"±
30	NB3009	G	1/16" 1/8" 1/8"	88'-11 1/8"	29'-0"	30'-11 1/4"	28'-11 7/8"	0	12.17"	7 #5@12"±	14 #5@16"±	18 #5@24"±	14 #5@16"±	7 #5@12"±

(b) Strand profile information

Figure 3: Girder section details for span 30NB of I-85

Fire hazard characterization

The inventory method is applied to quantify the combustion energy and heat release rate of the fire hazard. Figure 4, which was obtained from Google Earth street view images from February 2017, shows the stacks of high-density polyethylene conduits stored under span 30NB prior to the fire event. The width of three stacks of reels is approximately equal to the pier spacing at the bent as shown in Figure 4a; a distance of 26.7 ft. Vertically, the height of three stacked reels equals approximately half of the clearance, which is 12 ft. Based on this information, the reel size is most likely to be 102 in. (outside diameter) × 42 in. (inner diameter) × 48 in. (outer reel height). The diameter of the conduit outside cross-section is 2 in., according to the NTSB accident report [5], and the length of the conduit in each reel is 4500 ft. Moreover, the arrangement of the conduits is presented in Figure 5. The number in the circles indicates the number of conduit reels in each stack. Based on available information, it is presumed for this evaluation that 69 total reels were located underneath span 30NB during the 2017 fire event.

Both fiberglass and HDPE conduit were stored under the bridge. The stored materials were evaluated for flammability using the UL-94 test after the fire event. The UL-94 test consists of a horizontal flame test where a flame is applied to the free end of the specimen until ignition and then removed. If the material stops burning before 100 mm of length is ignited, it passes the HB classification. According to the NTSB report [5], the fiberglass conduit material does not meet the UL-94 flame classification HB and will continue to burn. The HDPE meets the UL-94 HB flame classification but liquefies when exposed to sufficient heat, thus resulting in fire spread through the dripping or flowing of the flaming polymer liquid. For the thermal load quantification, the HDPE conduit combustion properties are used. The heat of combustion of polyethylene material is 43.3MJ/kg per the SFPE handbook [26], while the mass loss rate for polymer liquid is 0.026 kg/m^{2}s^{-1}. Overall, the approximate heat release rate per unit area is taken as 1.12 MW/m^2.

Based on Google Earth street view images, the assumption is made that the majority of the stored material consists of reels of HDPE. The assumption is made that the top of each reel stack is on fire and producing the flame height and primary heat release rate. The aggregate top of reel combustion area is estimated at 107.5 m^2 (stacks of 25 reels per Figure 5 with outer diameter of 102 in. and inner diameter of 42 in., or 4.3 m^2 combustion top area per stack), which yields a maximum heat release rate of $\dot{Q}_{f,max}$ = 120 MW. Accordingly, the flame height H_f can be calculated using one of several semi-empirical expressions that are available in the current literature, such as Heskestad's correlation [27]:

$$H_f = 0.235\dot{Q}_{f,max}^{0.4} - 1.02D_{f,eff} \tag{1}$$

where $\dot{Q}_{f,max}$ (kW) is the peak heat release rate and $D_{f,eff}$ (m) is the effective fire diameter that can be calculated via Eq. (2) as follows.

$$if\ \frac{L_f}{W_f} \leq 2.5, D_{f,eff} = \sqrt{\frac{4A_f}{\pi}}; \tag{2a}$$

$$else, D_{f,eff} = \sqrt{\frac{4\left(2.5 \cdot W_f^2\right)}{\pi}} \tag{2b}$$

where A_f (m^2), L_f (m) and W_f(m) are the area, length (long edge dimension), and width (short edge dimension) of the rectangular pool fire footprint, respectively. Conservatively, the entire combustion plan area of the conduit stacks is assumed to be on fire, yielding a flame height of 13.5 m (44.9 ft). Hence, the PS concrete girders are engulfed in flame. As the HDPE material is liquefied in the combustion process, the thermal input for the subsequent thermal-structural analysis could follow the standard test method of ASTM E1529 for determining the effects of large hydrocarbon pool fires on structural members and assemblies, either applying the temperature of 1095°C ± 85°C or heat flux of 158 kW/m^2 ± 8 kW/m^2 to the surface of the structure members. This represents the envelope or maximum thermal impact the structure members could experience when exposed to open-air hydrocarbon pool fire.

The bridge collapsed 1 hr and 9 min after the fire started, and fire crews had the blaze under control ~40 min afterward [5]. According to an inventory method takeoff evaluation, the conduit stored underneath the bridge could support an even longer combustion time. Hence, the thermal demand retains its upper bound value of 166 kW/m^2 until the time of bridge collapse. The assumed heat flux time history applied to the surface bridge girder is shown in Figure 6.

(a) View 1

(b) View 2

(c) View 3

Figure 4: Views of the conduit reels stored underneath span 30NB

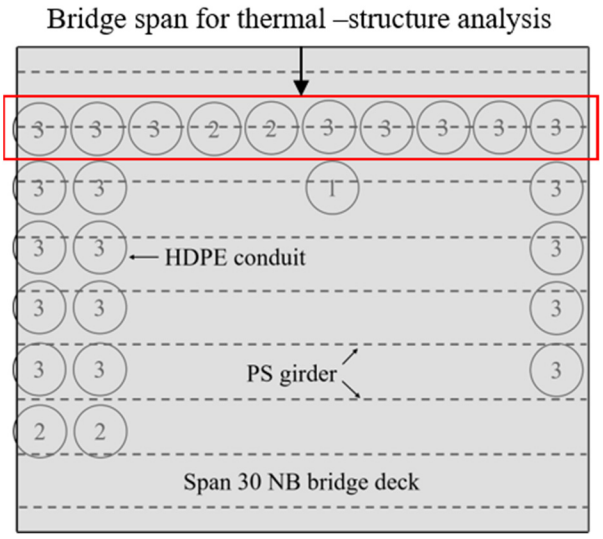

Figure 5: Arrangement of HDPE conduit reels stored underneath span 30NB

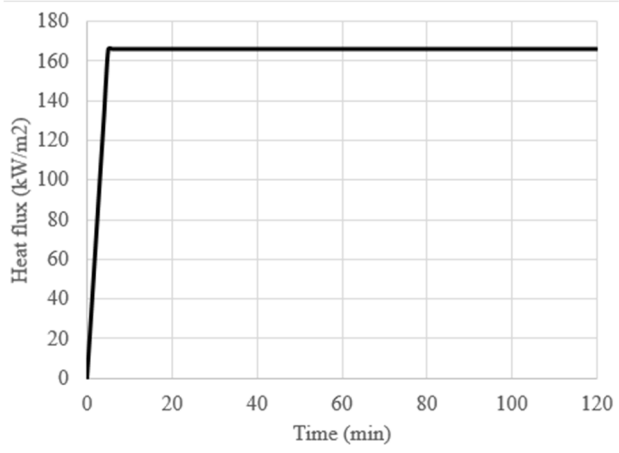

Figure 6: Time history of the assumed thermal load applied to the girder surface per ASTM E1529 (upper bound)

Gravity load for structure analysis

A summary of the gravity loading applied to span 30NB for this study is provided in Table 1. These loads are assumed to be distributed equally to the nine girders. The concrete weight assumes a density of 150 pcf and accounts for the concrete girder, deck slab, taper in the overhangs, haunches above the beams, and parapet. A wearing surface is assumed to provide an additional 25 psf over the 76.3-ft width of the roadway surface. Live load is conservatively represented using the 640 plf uniform longitudinal load for each lane in accordance with the AASHTO bridge design specification [4], and this bridge supports four lanes. This study does not include the concentrated truck live load with dynamic effects since heavy vehicles will most likely not be traveling across the bridge at full speed during the fire event.

Since fire is considered to be an extreme load scenario, a load combination with reduced live load is utilized for this evaluation. Though there is no prescribed load combination for the structural-fire analysis of bridges in US practice, several previous studies [7,13] have established DL + 0.3LL as a combination that is consistent with the guidelines in Eurocode 1 [28] for structural-fire analysis. These loads are applied as a constant distributed force along the length of the girders during the structural-fire evaluation, during which the full effects of fire exposure are also applied to the structural elements as a time history from ignition to burnout. Other load combinations that include wind, seismic, snow, rain, etc., are not considered to be likely during a severe fire event, and these loads are, therefore, not considered for this study.

Table 1: Summary of gravity loading on the sample bridge

Dead load	Calculation	DL Per Girder	Unit
Deck Slab	(150pcf)(79ft)(8.5in)/12/9	932.6	plf
Girder Self Weight		1055.0	plf
Barrier	2(330plf)/9	73.3	plf
Stay-in-place Forms	(15psf)72/9	120	plf
Haunch weight	(0.5in)(42in)/144(150pcf)	22.0	plf
Wearing surface	(25psf)(76.3ft)/9	212.0	plf
	Total DL per girder	2294.9	plf
Live load		LL Per Girder	Unit
Uniform Lane Load	(640plf/lane)(4 lanes)/9	284.4	plf
Load Combination		Load Per Girder	Unit
DL+0.3LL		2500.22	plf

Thermo-structural analysis for flexure capacity

The thermo-structural analysis of the PS concrete bridge is performed using the finite fiber element method in SAFIR 2019.a6 [29]. Per Figure 5, the girder framed in the red box is selected as the target bridge girder since the entire girder is engulfed in flame and experiences the most sever fire impact. Longitudinally, this composite bridge girder (bulb-T girder + bridge deck) is divided into small segments with a unit length of 2 ft. For thermal analysis, each segment cross-section is discretized into numerous 2D fiber elements and analyzed as exposure to the heat flux time history shown in Figure 6. In this process, the spalling of the concrete is simulated by progressively removing the surface elements, which is introduced in the following section. Then, the structure performance of the composite bridge is simulated using the 2D fiber-beam element, reading the temperature field obtained in the thermal analysis. The prestress is implemented as the initial stress in the elements representing the strands.

Thermal spalling simulation

Fire-induced concrete spalling has been broadly studied in past decades [30–33], with various experimental testing programs using cylinders [34–36], small panels [34,37,38], and larger structural elements [39–41] under high-intensity heating in furnaces or from radiant panels. A recent review of spalling behavior test results [42] identifies the following contributing factors for thermally-induced explosive concrete spalling: increases in mechanical stress due to restraint of thermal elongation and from applied loads, increases in pore pressure due to phase change of free and chemically bound water in the concrete matrix, and thermally induced reductions in the concrete strength. Methods to predict spalling, ranging from simple design thresholds [43,44] to complex numerical solutions [45–54] or the use of artificial intelligence [55,56], have been developed based on the results of experimentation. However, there is still no widely accepted prediction methodology that can accurately describe the concrete spalling phenomenon in terms of timing and depth (or if it will occur at all) [57].

The implementation of fire-induced concrete spalling in this study utilizes a semi-empirical prediction based on recent experimental testing by the authors on normal-weight concrete (NWC) panels under severe one-side thermal exposure [3]. As long as the concrete surface has moisture content by mass greater than 2.4% and a non-zero amount of applied compressive stress or restraint to thermal expansion, the results of those tests indicated that explosive spalling would be triggered once the concrete surface temperature reached 450°C. The sudden, explosive loss of concrete would generally penetrate to a depth where the concrete temperature was 150°C. Since this prediction is purely based on temperature, it can be overlaid onto a thermal FE analysis in an iterative procedure (inspired by that previously proposed by Hua et al. [42]). Note that this spalling prediction is applied deterministically in this study since more data beyond the previous study by Carlton et al. [3] would be needed to adequately develop a stochastic prediction.

As shown in Figure 7, in the first iteration of thermal FE analysis, the undamaged model is subjected to the full-time history of one-sided thermal exposure. The results of the initial analysis are then scanned by a custom MATLAB script, which identifies the time step at which the 450°C temperature threshold has been reached in the outermost concrete layer. At that time step, all concrete layers to the 150°C depth are instantaneously removed from the model, and the MATLAB script restarts the thermal analysis in SAFIR for the remainder of the heating time history. The restarted analysis retains the thermal state from the previous time step for all remaining fibers, and the thermal heating frontier is now applied to the newly exposed layer at the spalled depth. Once completed, the results of the restarted analysis are again scanned by the MATLAB script, and subsequent spalling via additional layer removal and another restart of the thermal analysis is implemented if the newly exposed concrete surface reaches 450°C.

This iterative process continues until the full heating time history has been completed with no additional spalling. Note that the maximum possible spall depth for any heating regime is assumed to be capped at the depth to the outermost reinforcement (i.e., the concrete cover layer). This maximum spall depth is consistent with modeling guidance in Eurocode 2, Part 1-2, which states that the concrete cover can be removed from the onset of analysis as a conservative approximation of spalling [58]. This guidance is predicated on the assumption that the reinforcement will likely provide at least some restraint to impede further advancement of spalling. Figure 7 demonstrates the implementation of the iterative SAFIR-MATLAB spalling procedure to the reinforcement depth, which is marked with a blue line for illustrative purposes (i.e., the blue line does not indicate a fiber).

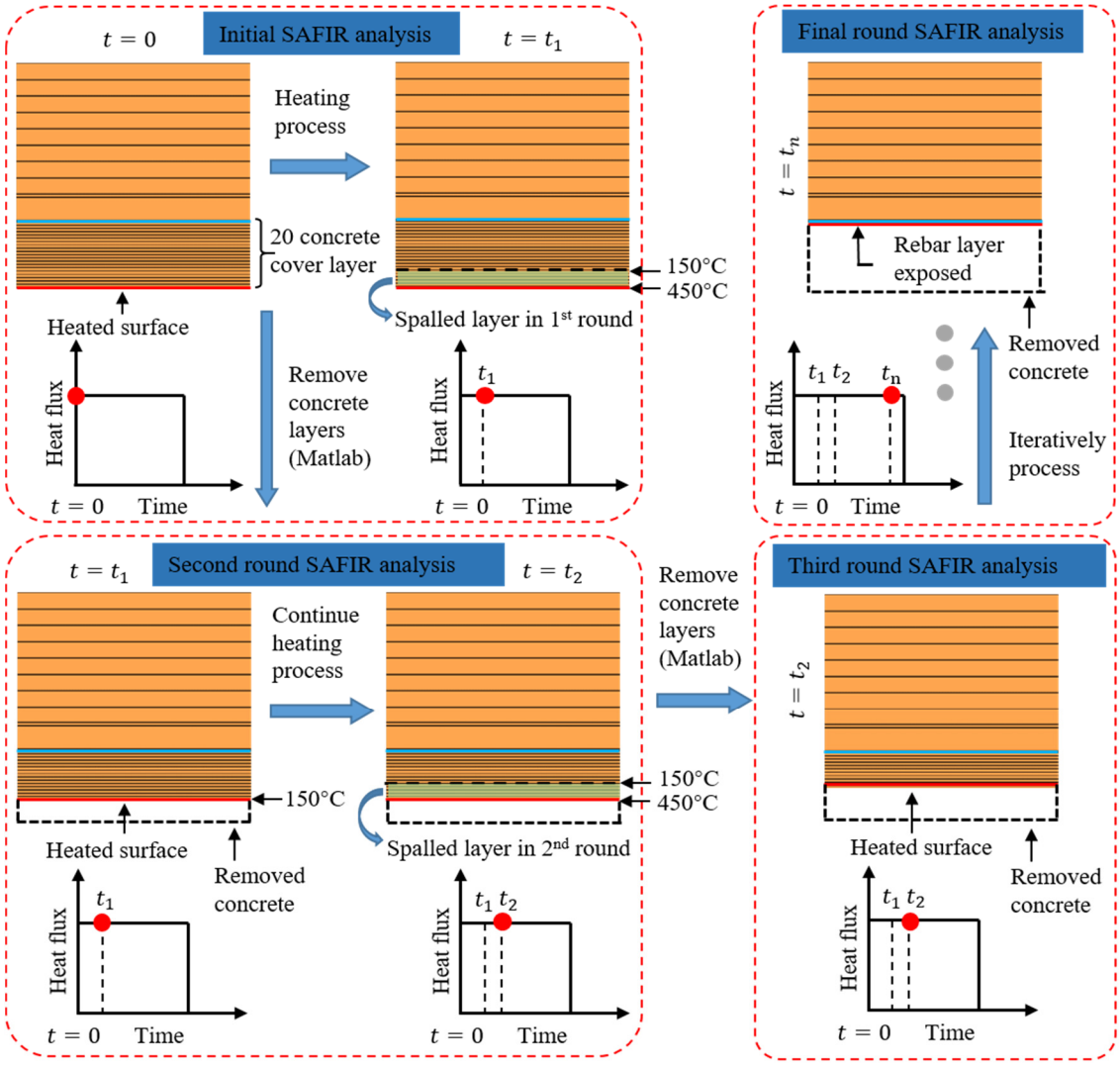

Figure 7: Illustration of the iterative SAFIR-MATLAB thermal FE analysis approach, including thermally induced spalling

Thermal analysis for prestressed concrete girder with the composite deck

Per Figure 8, the composite girder cross-section is modeled for thermal analysis. The effective width of the composite bridge deck is taken as the girder-to-girder spacing. Since the target girder is engulfed in the flame, the heat flux curve per Figure 6 is applied to the entire exposed beam perimeter and deck soffit, as shown in Figure 8. The strands and reinforcement embedded in the cross-section are represented with squares with area equivalency at the locations following the shop drawing in Figure 3. Meshing this cross-section is performed using the software GID 13 [59], which provides a robust pre and post-processing system for finite element analysis. The entire cross-section is meshed with quadrilateral elements. To simulate the spalling process, the concrete cover with thickness ranges from 1.75 in. (at the web location) to 2.0 in. (at the bottom flange) is consistently discretized into ten layers. For other locations, an approximate element edge length of 0.5 inches is applied. In total, this cross-section contains around 22,000 elements, which is adequate to capture the thermal penetration and temperature elevation of this girder. Note that Figure 8 represents the arrangement of the strands and reinforcement and mesh for the cross-section at midspan. To model the harping of five strands, as shown in the elevation details of Figure 3, for subsequent structure response simulation, the entire bridge span is evenly discretized into 46 elements (with a unit length of 2 ft). The five harped strands change their positions along the girder and are framed with the solid red box, as shown in Figure 9. Hence, the thermal analysis, including the spalling simulation, should be applied to each discretized element.

The reinforcement and prestressing strand in the bridge deck and PS concrete girder are modeled using temperature-dependent thermal properties, including thermal conductivity, specific heat, and density, per Eurocode 3 [60]. The concrete material for both the deck and concrete girder is assumed to have 46 kg/m^3 water content, while its thermal conductivity is assumed equal the Eurocode 2 [58] mean temperature-dependent relationship for siliceous structural

concrete [58]. Convective coefficients for the fire-exposed and unexposed surfaces are 25 kW/m^2 and 9 kW/m^2 per Eurocode 1 [28]. Heat radiation, incorporated into the numerical model, uses an emissivity factor of 0.7 and a Stefan–Boltzmann constant value of 5.67×10^{-8} W/(m^2-K^4). A resultant emissivity, ε, equal to 0.52 for all exposed and unexposed surfaces of the cross-section is calculated via Buchanan's Eq. 3.20 [61]:

$$\varepsilon = \frac{1}{1/_{e}+1/_{r}-1} \tag{3}$$

where ε_e is the emitting surface and ε_r is the receiving surface.

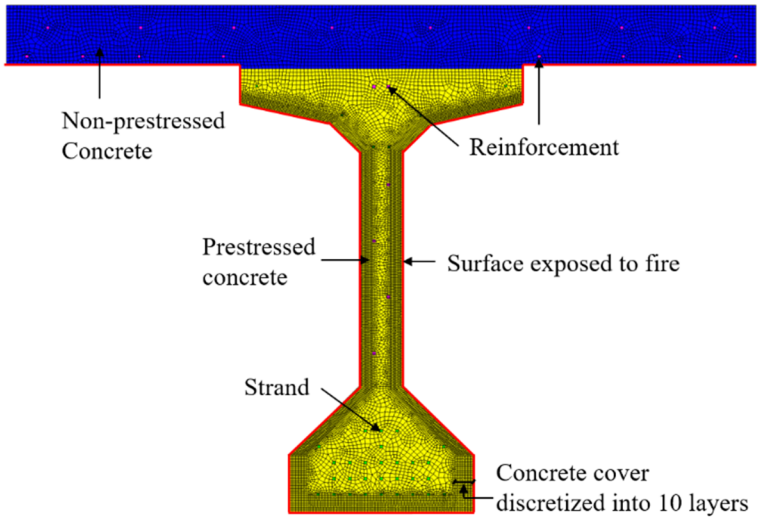

Figure 8: Cross-sectional model for thermal analysis of the Span 30NB girder

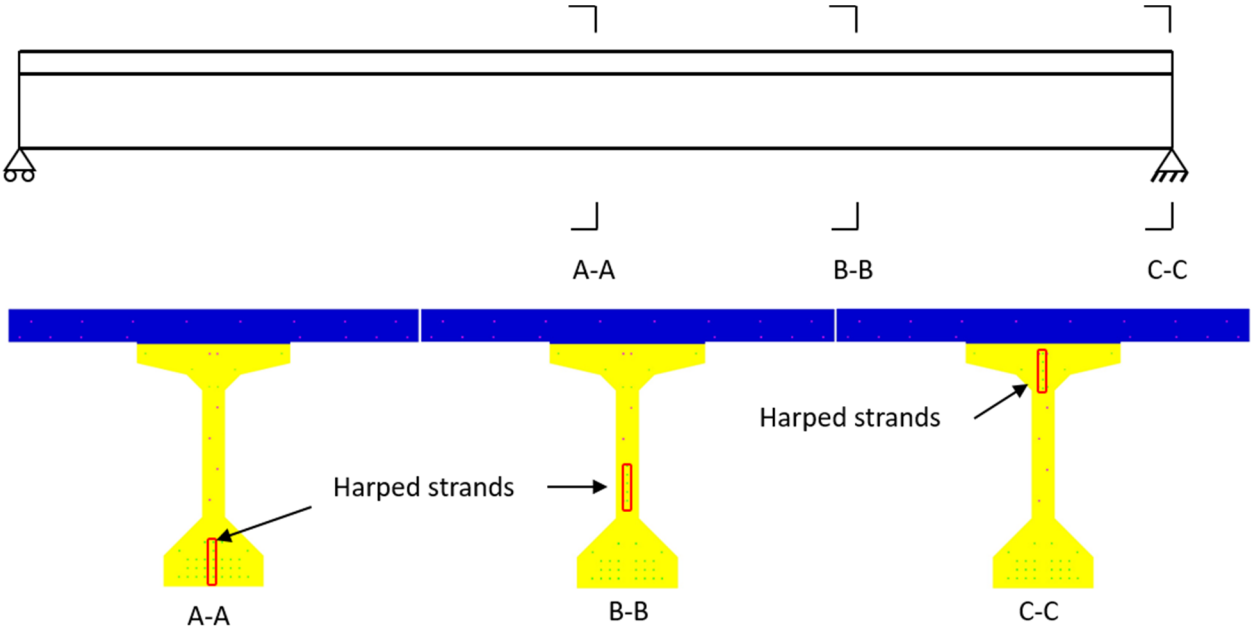

Figure 9: Longitudinally harped strands in the girder cross-sectional model

The spalling process of the concrete cover for the entire cross-section is illustrated in Figure 10. To save the computation power, one layer or several layers of concrete cover is/are removed from the thermal analysis model consistently along the girder's perimeter if the spalling threshold is reached, as described in the previous section. The temperature at two locations, one on the web and one on the bottom surface of the girder, are recorded for spalling simulation. For example, if the average surface temperature of these two locations exceeds 450°C, then spalling is triggered. The concrete cover is spalled to the layer with an average temperature of 150°C. Figure 10 presents the spalling process as the girder is exposed to the heat flux time history in Figure 6. The region framed in the red dash line box is amplified to present the spalling process more clearly. In the analysis, the concrete cover first spalls at 210

sec (3 mins 30 secs) and requires the removal of the two outmost layers from the thermal analysis model. Subsequently, the spalling happened four additional times at t = 270 sec (4 mins 30 secs), 320 sec (5 mins 20 secs), 370 sec (6 mins 10 secs), and 420 sec (7 mins); the thermal demand required that two layers of the concrete cover were removed at each of these time steps. Once the steel reinforcement layer was reached, no additional removal was conducted at that location. Some strands, such as those located at the bottom of the flange, are directly exposed to the thermal impact, resulting in a significant temperature increase in the following heat/spall process.

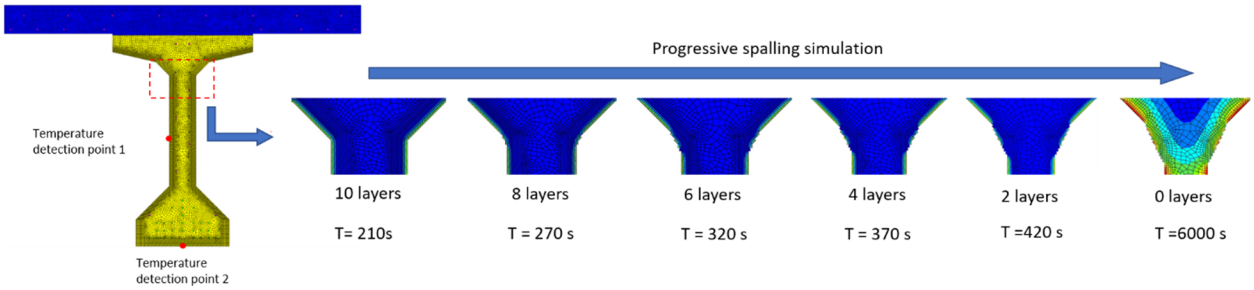

Figure 10: Thermal spalling process of the I-85 girder

Figure 11a illustrates the temperature distribution of the spalled concrete girder 14 ft from the middle span (element 30) at 78 min after the fire starts, while Figure 11b presents the temperature-time history curve for selected strand fibers. It could be noticed that the temperature elevation of all the strand fibers accelerates around 7 minutes after the fire starts, which is consistent with the time that the whole concrete cover is spalled from the girder, according to Figure 10. The temperature of Fiber 1, which is located at the bottom of the girder cross-section, increases dramatically since it is directly exposed to the fire. Around the time that the bridge collapsed (1 h 9 min), Fiber 1 has reached 1150°C, which could reduce the strength to less than 1% of the strength at normal temperature. For the strand fibers harped into the web (i.e., Fiber 4 to Fiber 6), the temperature increase is not as intense as Fiber 1 but still reaches 1000°C, which also compromises the strands after 1 hr of heating. Fibers 2 and 3, which are located at the junction of the bottom flange and the web, are protected by more concrete. Correspondingly, the temperature of these two elements reaches 400°C and 720°C, respectively, yielding their strength to 13% and 3% of the strength at normal temperature. In general, the harped strands in the region from 0.6*L*-0.8*L* located in the web of the concrete girder experience a temperature exceeding 900°C (could be indicated by the orange color in Figure 11a), which does impact their strength and the capacity of the PS concrete girder.

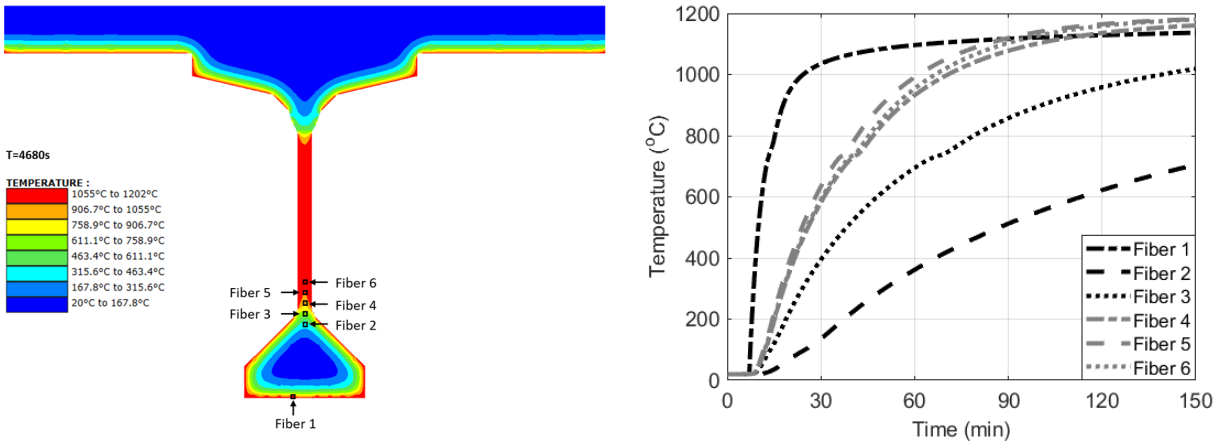

(a) Temperature distribution at t = 78 min

(b) Temperature time history of selected fibers

Figure 11: Thermal analysis result of the prestressed girder of element 30

Structural response

As aforementioned, the strands conform to ASTM A416 [24] Grade 270 and are pretensioned to 28,910 lbs each (~65% of nominal tensile strength). The mild steel reinforcement conformed to ASTM A615 [25] Grade 60. All steel elements are assumed to have a density of 490 pcf. For the prestressed concrete, the compression strength is 5,000 psi, while the strength for the reinforced concrete (i.e., bridge deck) is 3,500 psi. The tension strength of concrete is assumed to be negligible.

When heated by fire, both steel and concrete will experience a temperature increase accompanied by a loss of strength and stiffness as well as thermal expansion. The stress-strain relationships of these materials will also become increasingly nonlinear. Some guidance exists in current North American standards for calculating the performance of these materials at high temperatures, such as Appendix 4 in AISC 360 [62], ACI 216 [63], and the ASCE Manual of Practice 78 [64]. However, the Eurocode is currently the most widely recognized standard for structural-fire evaluation in a majority of construction markets worldwide since it comprehensively addresses the thermal and mechanical material properties of structural steel, multiple concrete types, rebar, etc. Even some of the current US standards, such as Appendix 4 in AISC 360 [62], use material reduction factors that are very similar to corresponding portions of the Eurocode.

High-temperature properties for steel rebar are assumed to conform to Eurocode 2 Part 1-2 [58] with hot-rolled Class N reduction factors for strength and stiffness and Class A ductility (low) to match the maximum tensile strain at ambient conditions for ASTM A615 [25] (at just less than 10%). The reduction factors for rebar according to Eurocode 2 [58] are shown in Figure 12a, and the stress-strain relationships are presented in Figure 12b with a maximum strain of 10%. In SAFIR, the reinforcement is modeled using the material model STEELEC2EN [65].

The strength and deformation properties of prestressing steel at elevated temperature adopt the parameters for cold worked Class B type also from Eurocode 2 Part 1-2 [58] and are simulated with PSTEELA16 [65] material model in SAFIR. Compared to the reinforcement, the strength reduction of the prestressing steel is more significant per Figure 13a. Note that $\beta = 0.9$ is applied to the specified tensile strength f_{pk} to calculate the yield strength of the strand of Class B type. The temperature interval that has minor or no influence on the strength is below 100 °C. When the temperature of the strand exceeds 600°C, the strength decreases to 10% of the value at ambient temperature. For the reinforcement, this threshold occurs at 900°C. The limited strain for yield strength and ultimate stain increases with the temperature per Figure 13b.

The thermo-mechanical properties of the concrete for both the bridge deck and prestressed girder adopt the material model of normal strength concrete with siliceous aggregates, which is consistent with the thermal analysis model. The reduction factor applied to the compression strength and the strain-stress relation of this type of concrete is presented in Figure 14 per Eurocode 2 [58]. The transient creep is treated as explicit in the model. Hence, the SILCON_ETC [65] in SAFIR is selected. The explicit formulation is a refinement of the model calibrated to yield the same response as the current Eurocode model in the purely transient situation. This explicit formulation is able to account for the non-reversibility of transient creep strain when the stress and/or the temperature is decreasing [66].

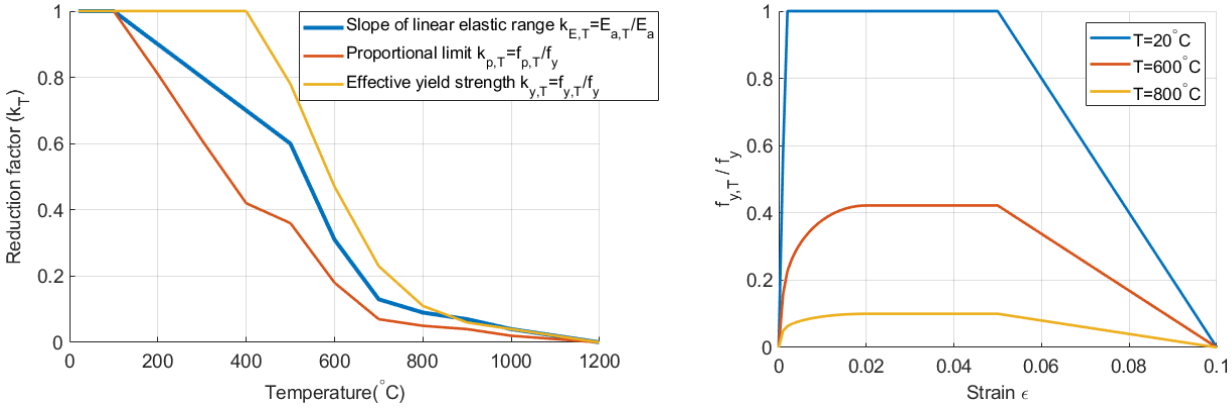

(a) Reduction factors at elevated temperature

(b) Stress-strain relationships

Figure 12: Thermal and mechanical properties of hot-rolled Class N reinforcement per Eurocode 2 [58]

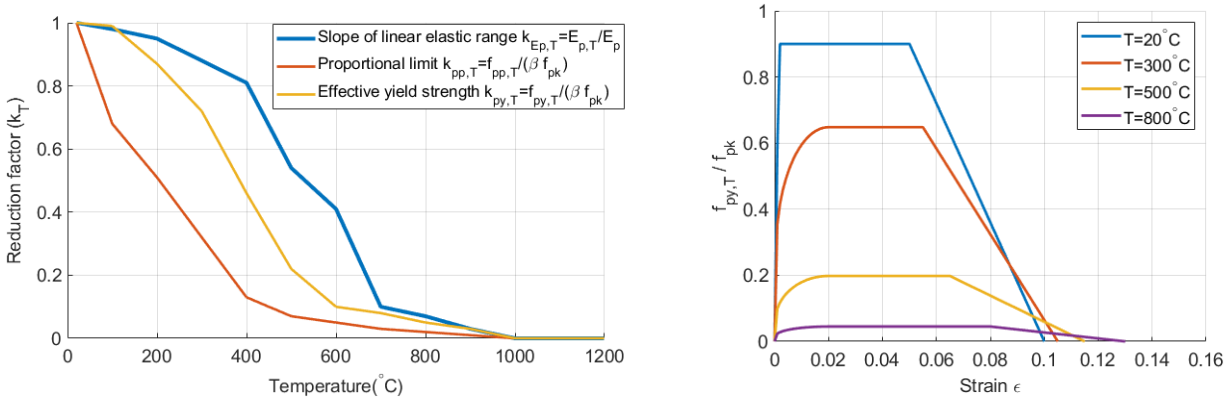

(a) Reduction factors at elevated temperature

(b) Stress-strain relationships

Figure 13: Thermal and mechanical properties of cold-worked Class B strand per Eurocode 2 [58]

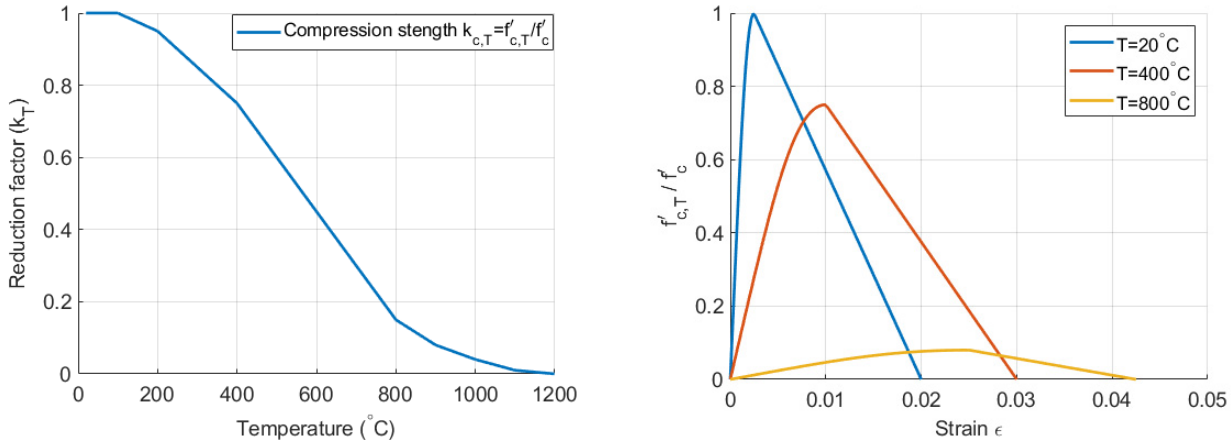

(a) Reduction factor

(b) Stress-strain relationships

Figure 14: Thermal and mechanical properties of siliceous concrete per Eurocode 2 [58]

The uniformly distributed load calculated per Table 1 is applied onto the target fiber element girder, as shown in Figure 5, for structural analysis. The entire girder is engulfed in the flame. This gravity load is conservatively assumed to be constant throughout the fire event. The boundary condition is idealized as a pin-roller for the simply supported beam, as shown in Figure 15a or Figure 9. The deformation of the girder at 78 min at 10x magnification is presented in Figure 15a. It is the time interval that no convergence is captured in the finite element analysis and can be considered as the failure time of the bridge. It is close to the collapse time of this bridge span in the fire hazard in 2017, which is 1 hour and 9 minutes. The deflection time history at midspan is shown in Figure 16. It can be noticed that at the beginning phase of the fire loading, the displacement equals zero since the prestressed strands provide an equivalent distributed load upward. Before the whole concrete cover is removed from the model, the cross-section of the PS concrete girder retains its stiffness and moment capacity since the temperature of the strand is low. Once the concrete cover is removed (around 7 minutes per Figure 11b), the temperature of the directly exposed strands elevates significantly, which decreases the capacity of the PS concrete girder. It is not very obvious but still remarkable that the discontinuity of curvature at the location of element 30 circled in Figure 15a. This location is close to the presumed failure location of span 30NB (at 30% of the span length from the pier) that collapsed in the fire hazard, as shown in Figure 15b.

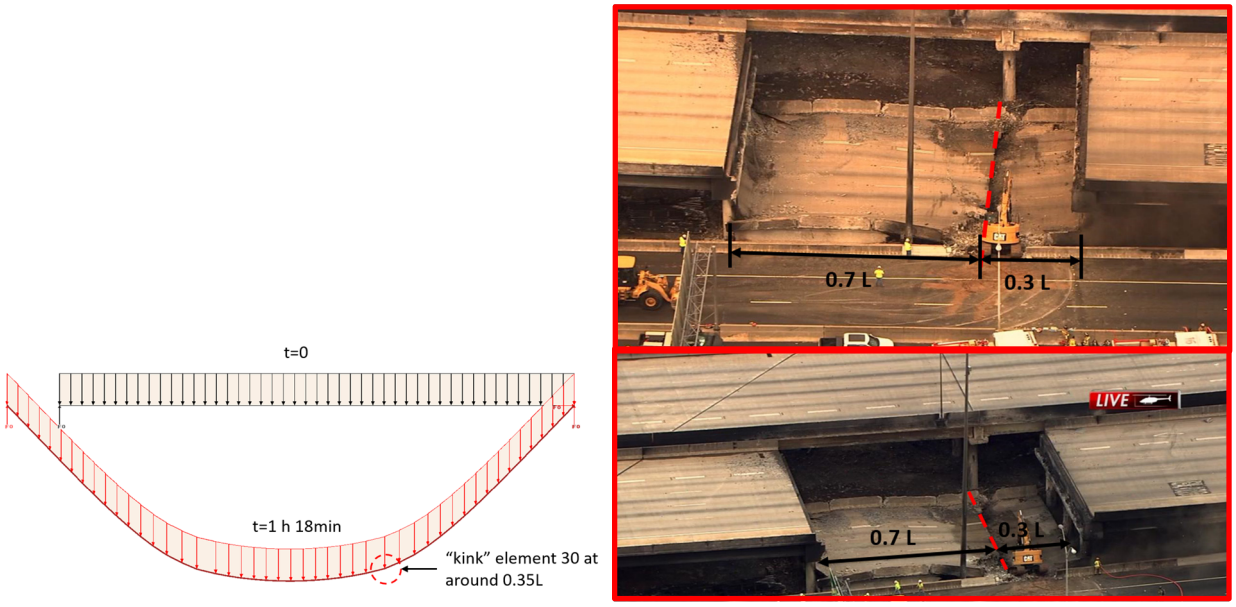

(a) Deflection of PS girder from FE analysis (b) Observations of damage location

Figure 15: Structural-fire response of span 30NB

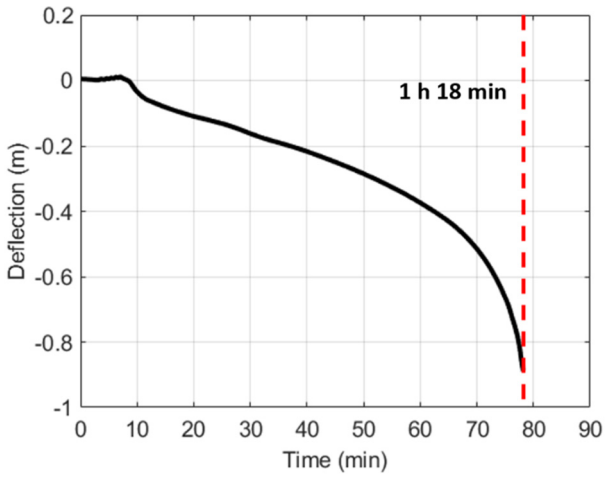

Figure 16: Deflection time history at midspan of the girder

A detailed investigation is conducted to understand the stress and capacity of the cross-sections along the girder in the fire hazard. Selected elements of interest are shown in Figure 17. The compression stress of the top fibers of the cross-section, as framed in Figure 18a, generally represents the state of the cross-section subjected to the applied moment. The higher this compression stress, the closer the cross-section is to flexural failure. Figure 18b presents the compression stresses time history curve of selected elements reading from the SAFIR output file. It should be noted that the compression stress decreases at elements closer to the support before the fire starts. As the cross-section begins to spalling and is heated at an increased rate, the compressive stress of the top fibers then increases since the heated strands cannot provide sufficient prestressing force. Among the selected elements, the stress increase rate of the "kink" element (element 30) accelerates around 40 min, which makes it the element with the highest top fiber compression stress and most likely to fail. This is because the harped strands at this location are in the web portion of the cross-section. After the onset of spalling, the web becomes thinner, which increases the thermal penetration to the strands, per Figure 11. On the contrary, these strands at the location of element 24 (midspan) are embedded in the bottom flange and protected by more concrete, as presented in Figure 9. Hence, the temperature of these strands remains lower. To summarize, the midspan is not the only location that matters for the prestressed concrete girder with harped strands. A location with less moment and a more thermally vulnerable cross-section (i.e., with strands harped into the web) also require careful investigation.

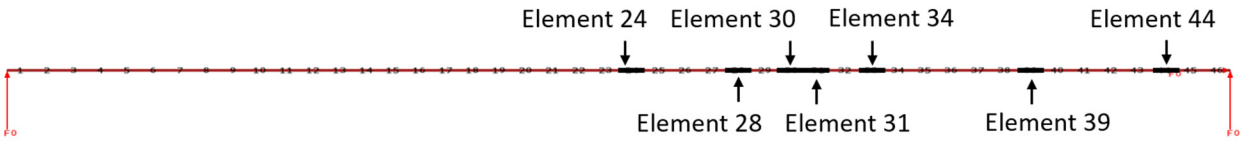

Figure 17: Element numbering along the girder FE model span

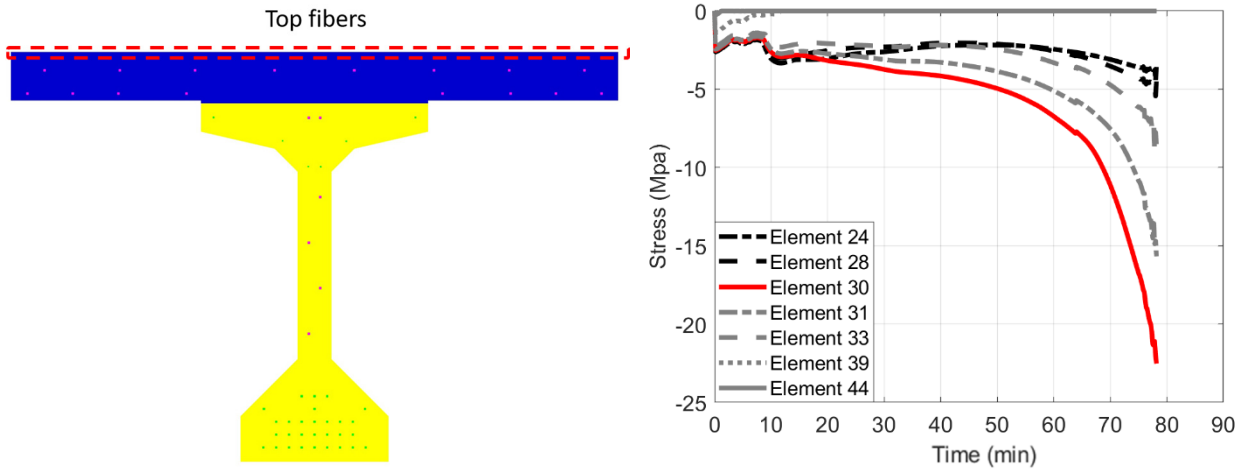

(a) Fiber location for investigation (b) Stress time history

Figure 18: Stress time history for the top fibers of the composite PS girder FE cross-section

The moment capacity of the thermally impacted cross-section is calculated by integrating the moment contributed by each fiber of the cross-section. Figure 19 shows the strain distribution of the cross-section for ultimate moment capacity evaluation. The maximum compressive strain of the bridge deck concrete is taken as $\varepsilon_{cu} = 0.003$. The strain of the strands at the bottom is $\varepsilon_{pu,T} = 0.15$, which corresponds to the ultimate strain of the prestressing steel at 1200°C per Eurocode 2 [58]. The location of the neutral axis, y_N, is then located and the strain of each fiber of the cross-section, ε_i, is calculated based on the assumption that the cross-section remains plane per Figure 19. With the strain-stress relationships of reinforcement, concrete, and prestressing steel at elevated temperatures introduced in the previous section (i.e., Figure 12, Figure 13, and Figure 14), the stress of each fiber $\sigma_{i,T}$ can be calculated. The moment capacity of the fire exposed cross-section can then be computed via Eq. (4):

$$M_C = \sum_{i=1}^{n} \sigma_{i,T} \times A_i \times (y_N - y_i) \tag{4}$$

where n is the total number of fibers of the cross-section and A_i is the area of fiber i.

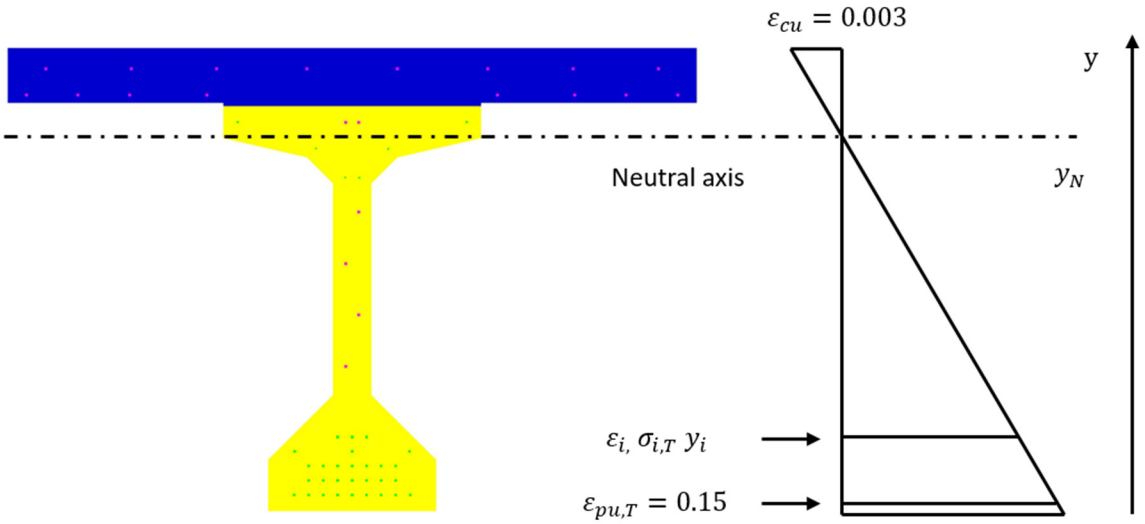

Figure 19: Strain profile of the cross-section for ultimate moment capacity calculation

The moment capacity of the cross-section gradually decreases when exposed to fire hazards, especially after the concrete cover is removed due to thermal spalling. Figure 20 plots the changes in moment demand vs. capacity with time for selected elements. The moment capacity of the "kink" element 30 (Figure 20c) drops to the demand value at the time of flexural failure. For all the cross-sections, the first significant drop (per Figure 20c) in moment capacity occurs right after the full removal of the concrete cover at 7 mins due to the direct exposure of the strand at the bottom location (which experiences significant temperature increase per Figure 11). The second and more minor decrease is attributed to the loss of stress of other strands embedded in the concrete. Compared to element 24 at midspan, the rate moment loss at the "kink" element 30 at the second phase is larger (i.e., approximately 34.6 kN-m/min for element 30 vs. 20 kN-m/min for element 24) since the harped strands in the web experience higher temperatures due to increased thermal penetration. Element 28 does not reach the failure threshold since the harped strands are still in the bottom flange and protected by more concrete. Element 31, which is next to element 30, also has a high potential of failure since its capacity almost reaches the demand value at the failure time. Though the harped strands of element 39 also experience high temperatures, the moment demand for this location is not significant, which makes this element not as critical as element 30. Per Figure 21, which shows the moment capacity vs. demand along the girder, the critical region in which the capacity decreases to the demand value is framed with a gray dash box. In summary, this numerical simulation approach can effectively predict the failure time and detect the failure location of span 30NB.

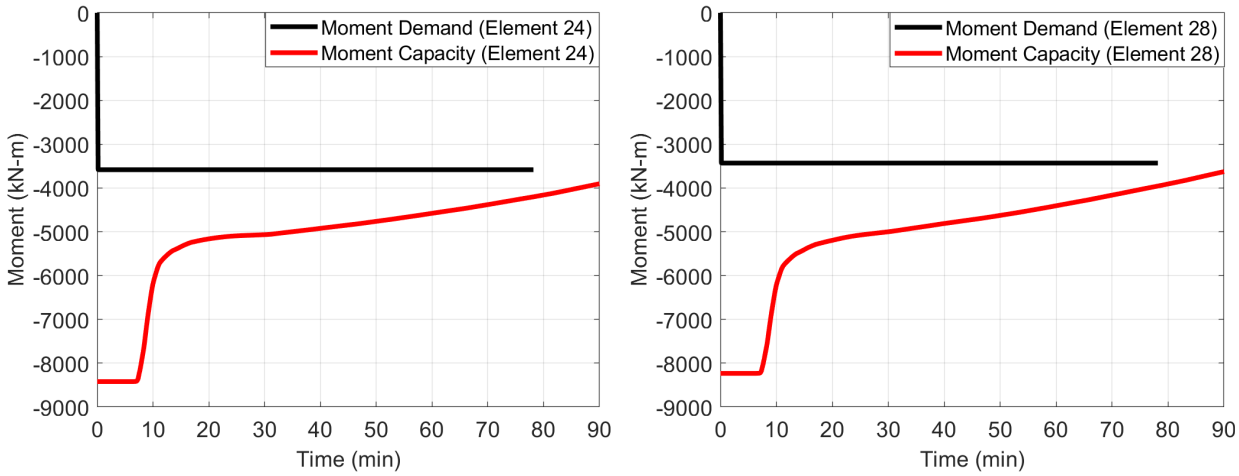

(a) Element 24

(b) Element 28

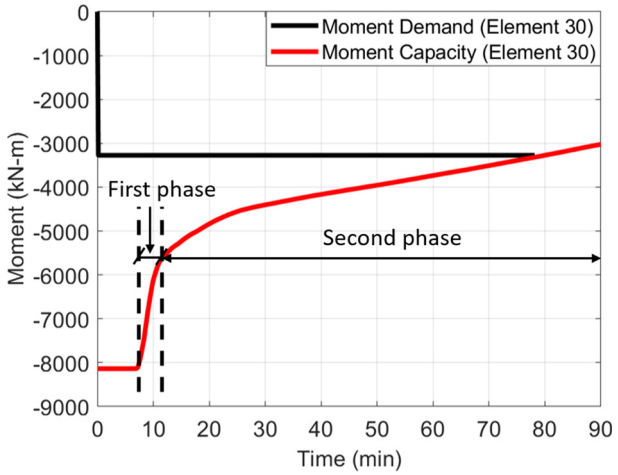

(c) Element 30

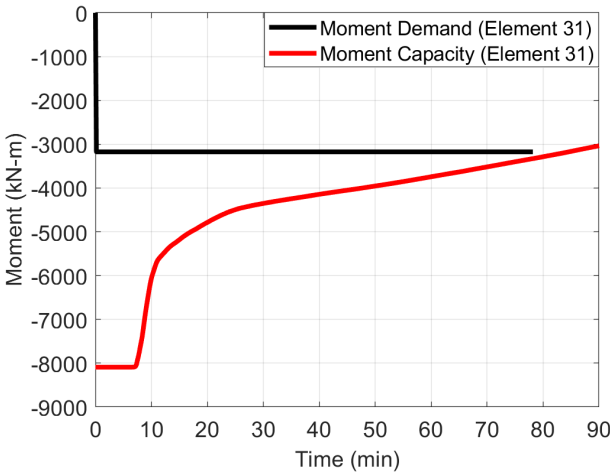

(d) Element 31

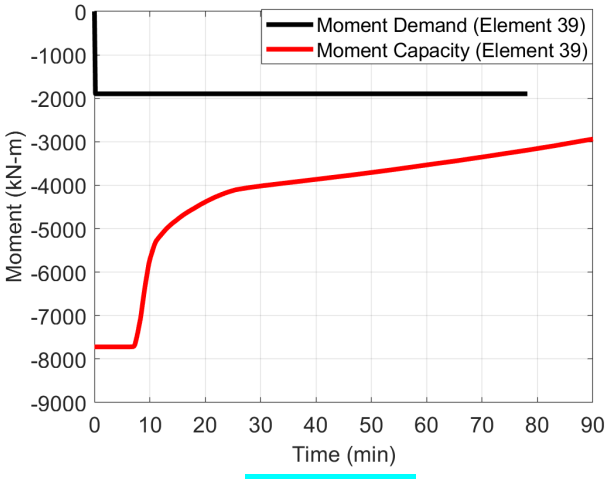

(e) Element 39

Figure 20: Moment capacity vs. demand time history for selected elements

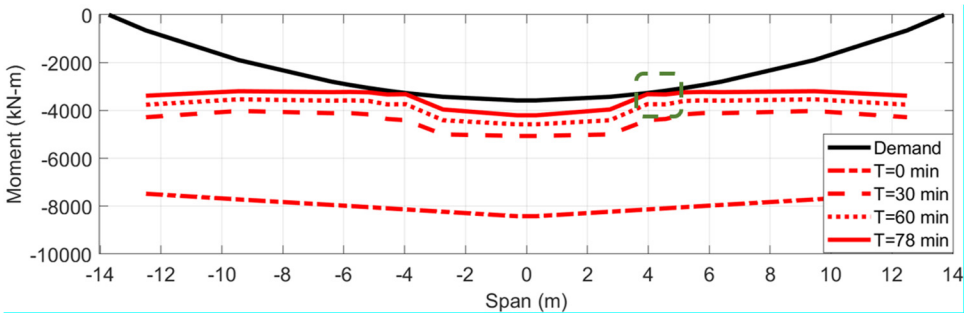

Figure 21: Moment capacity vs. demand along the girder at various time milestones

Shear failure check

The shear failure close to the support is another failure mode that requires investigation. The shear capacity evaluation of the cross-section generally follows the method in Chapter 5 of the AASHTO LRFD bridge design specification [4] but is modified to account for the effect of the thermal impact. The shear capacity of the prestressed girder with harped strands consists of the contribution from (1) concrete V_c; (2) shear reinforcement V_s and (3) harped prestressing steel V_p. The summation of three components multiplied by the resistance factor should be greater than the factored shear force V_u, which could be expressed by Eq. (5). Eqs. (6) through (8) provides the fiber base equation to calculate these components in the fire hazard.

$$\frac{V_u}{\phi} < V_c + V_p + V_s \tag{5}$$

$$V_c = 0.0316\beta \sum \sqrt{f'_{cT,i}} A_{c,i} \tag{6}$$

$$V_s = \frac{A_v f_{yh,T} d_v (cot\,\theta + cot\,\alpha)(sin\,\alpha)}{s} \tag{7}$$

$$V_p = \sum k_{pyT,i}\, f_{pu} A_{ps,i}\, sin\,\psi \tag{8}$$

where ϕ is the resistance factor (taken equal to 0.9 for design purposes but taken as 1 for a failure check); β is a factor indicating the ability of diagonally cracked concrete to transmit tension; $f'_{cT,i}$ is the compression strength of concrete element i in the area framed out with the red dash box in Figure 22 at elevated temperature; $A_{c,i}$ is the corresponding area; A_v is the area of shear reinforcement within a longitudinal spacing s (equal to 6 in. at the support according to the shop drawing); $f_{yh,T}$ is the specified yield strength of vertical reinforcement (refer to Figure 22) at elevated temperatures. Note that the shear reinforcement is not modeled in the 2D cross-section for thermal analysis – the temperature of that reinforcement is represented with the average temperature of nodes right behind the longitudinal reinforcement in the web. The location of these nodes is along the blue dash line, as shown in Figure 22. Distance d_v is taken between the resultants of tensile and compression forces; α is the angle of inclination of transverse reinforcement to the longitudinal axis and equals 90° for vertical stirrups. θ is the angle of diagonal compression; $k_{pyT,i}$ is the strength reduction factor of the strand fiber i at elevated temperature; f_{pu} is the ultimate strength of the prestressing steel at ambient temperature; $A_{ps,i}$ is the corresponding area; and ψ is the angle of harped strands to the longitudinal axis.

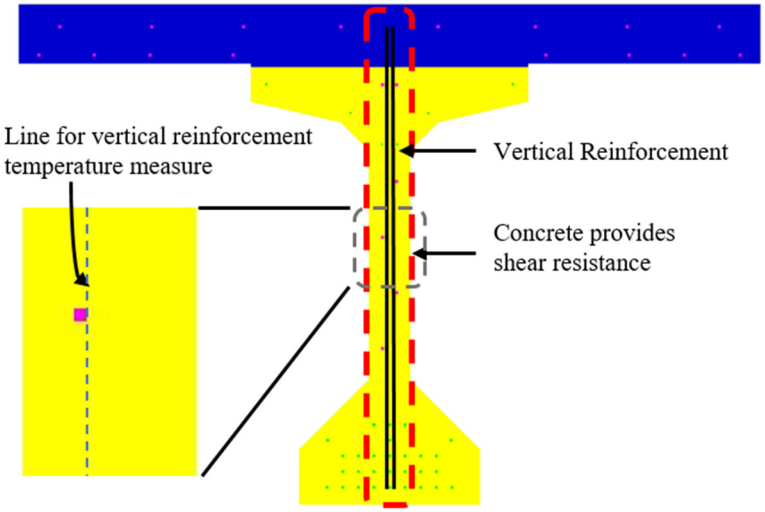

Figure 22: Cross-section of the girder for shear capacity quantification

Not only is the strength of the material (i.e., $f'_{cT,i}$, $f_{yh,T}$ and $k_{pyT,i}$) affected by the elevated temperature, but other parameters in these equations could be influenced as well. For example, the value of β is determined by the strain at the centroid of the tension reinforcement ε_s, which is calculated via Eq. (9):

$$\varepsilon_s = max[\frac{\frac{|M_u|}{d_v} + 0.5N_u + |V_u - V_p| - \sum A_{ps,i} k_{pyT,i} f_{po}}{\sum E_s k_{sET,i} A_{ss,i} + \sum E_p k_{pET,i} A_{ps,i}}, 0] \quad (9)$$

where M_u, N_u, and V_u are the applied bending moment, axial force, and shear force at the cross section evaluated for shear failure; E_s (E_p), $k_{sET,i}(k_{pET,i})$, and $A_{ss,i}$ ($A_{ps,i}$) are the modulus for reinforcement (strand) at ambient temperature, the reduction factor at elevated temperature of fiber *i,* and the corresponding area; f_{po} is the parameter taken as the modulus of the elasticity of prestressing tendons multiplied by the locked-in difference in strain between the prestressing tendons and the surrounding concrete and equals $0.7f_{pu}$. The values of M_u, N_u, and V_u slightly change during fire exposure, and the critical location for shear failure may migrate due to the thermal gradient. The factors that affect the critical location include (1) the height of the girder, which decreases slightly due to the thermal spalling at the bottom face; (2) distance from the extreme compression fiber to the neutral axis, which decreases as heated strands lose their strength; and (3) the effective centroid of the prestressing strands, which moves upward since any compromised strands are neglected, and any thermally weakened strands make less contribution.

The shear capacity time history at the critical location near the support is plotted in Figure 23 against the components of shear capacity. The capacity contributed by concrete (V_c) decreases in the first 10 min due to the spalling of the concrete cover at the bottom flange. With thermal penetration, the compression strength gradually decreases, reducing shear capacity. The vertical reinforcement provides the largest portion of the shear capacity (V_s) at ambient temperature. However, once the concrete cover of the flange is spalled, this portion is significantly reduced since the high temperature exposure compromises the vertical reinforcement. Though small, the portion contributed by the harped strands is not significantly influenced since those strands are in the top flange of the girder at this location and are well protected by the thicker concrete around them. Figure 23 shows that the shear capacity of the prestressed girder is significantly impacted in the fire hazard but is not indicate as the governing failure mode of the span 30NB bridge in the 2017 fire hazard since it requires a longer time (1 hr 39 min) to be reached. Moreover, the location of shear failure would be closer to the support rather than the observed failure location at $0.3L$ from the support, as shown in Figure 15b.

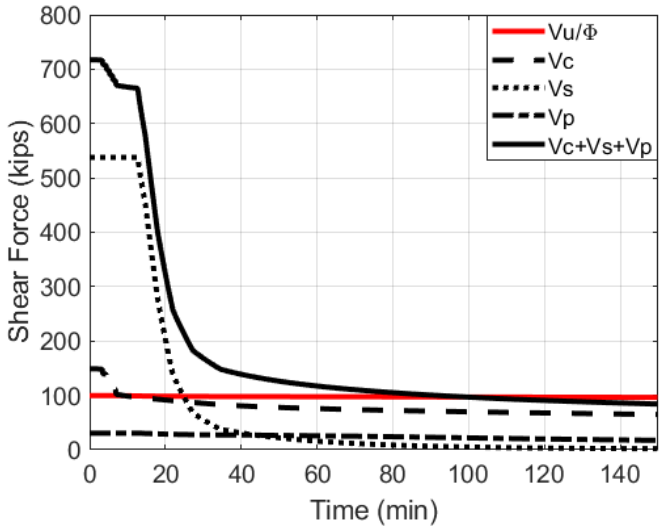

Figure 23: Shear capacity and demand at the cross-section near the support

Summary

This section presents numerical simulation approaches to investigate the thermo-structural response of the prestressed bulb-T concrete bridge girders subjected to fire hazards underneath. The effectiveness of these approaches is validated by modeling span 30NB of the I-85 bridge that collapsed due to the severe fire in 2017 in Atlanta, GA. The results of this analysis showed good agreement with the outcomes of the actual event. The failure mode of the span was indicated to be flexural runaway, and the simulation approach introduced in this report provided good predictions of the failure time and the mode of thermo-structural response for this bridge fire event. The harped strands in the web location can be heated to high temperature, which creates thermo-structurally vulnerable locations away from the midspan. The AASHTO LRFD specification-based shear capacity evaluation is used to check for shear failure since the vertical reinforcement could be thermally compromised due to fire-induced spalling.

Utilizing the numerical approach developed and validated for the Atlanta I-85 bridge collapse, the performance of a prototype PennDOT PS girder bridge is examined. The prototype system is composed of four bulb-T beams supporting a composite reinforced concrete deck. The prototype was chosen from the existing PennDOT bridge inventory and has a similar span as the aforementioned I-85 overpass. Figure 24 shows the plan view and cross-section of the PennDOT-provided prototype bridge, and Figure 25 provides detailed information of the arrangement of the strands and reinforcement in the girder cross-section. This study focuses on the longest span, which is 91'-2.5", as the target bridge for fire resilience analysis. A parametric study is conducted where the vertical clearance is varied from 15 to 45 ft. The girders of this prototype bridge are PennDOT BT-72, which are larger than the bulb-T girders used for the aforementioned I-85 interchange. Moreover, the section utilizes 56 ½-in. regular low relaxation 7-wire strands that conform to ASTM A416 Grade 270 [24]. No debonding is considered at the ends of the pretensioned girders and the strands are straight with no variation in eccentricity along the span. The strands have an initial prestress of 70% f_{pu} (the minimum tensile strength of the strand) or 28.9 kips per strand. The design compression strength of the concrete at 28 days is 5500 psi. The reinforcement conforms to ASTM A615 Grade 60 [25]. For the subsequent thermo-structural analysis, the gravity load on the girder quantification follows the combination of DL + 0.3LL, which is consistent with the guidelines presented in Eurocode 1 [28] for structural-fire analysis, as shown in Table 2.

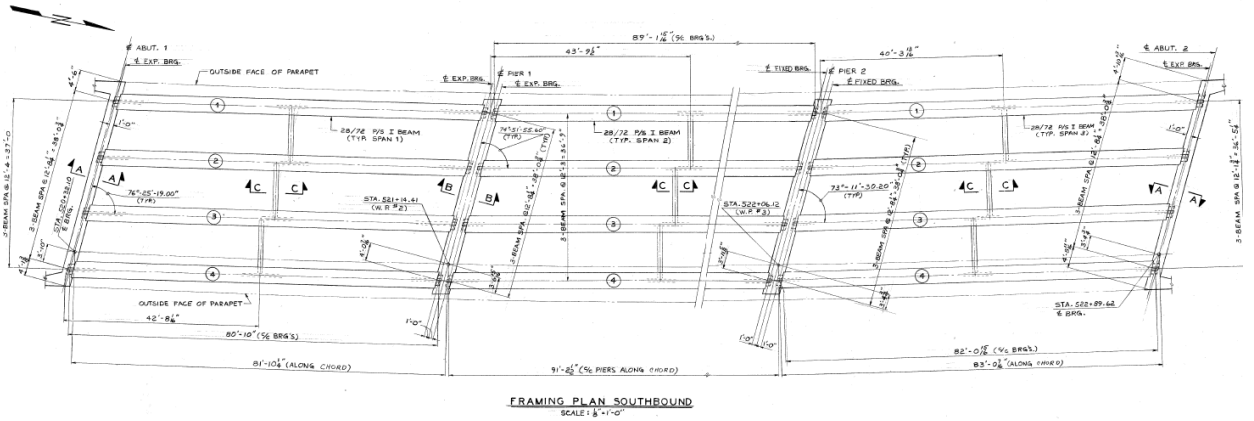

(a) Plan view

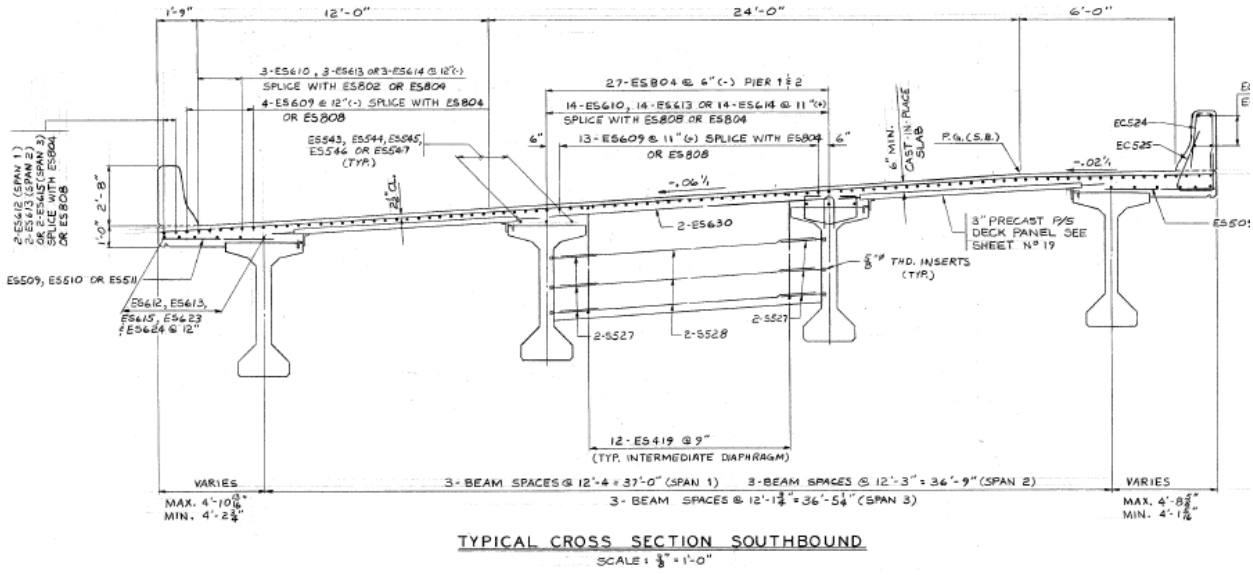

(b) Cross-section

Figure 24: Design drawings of the PennDOT sample bridge

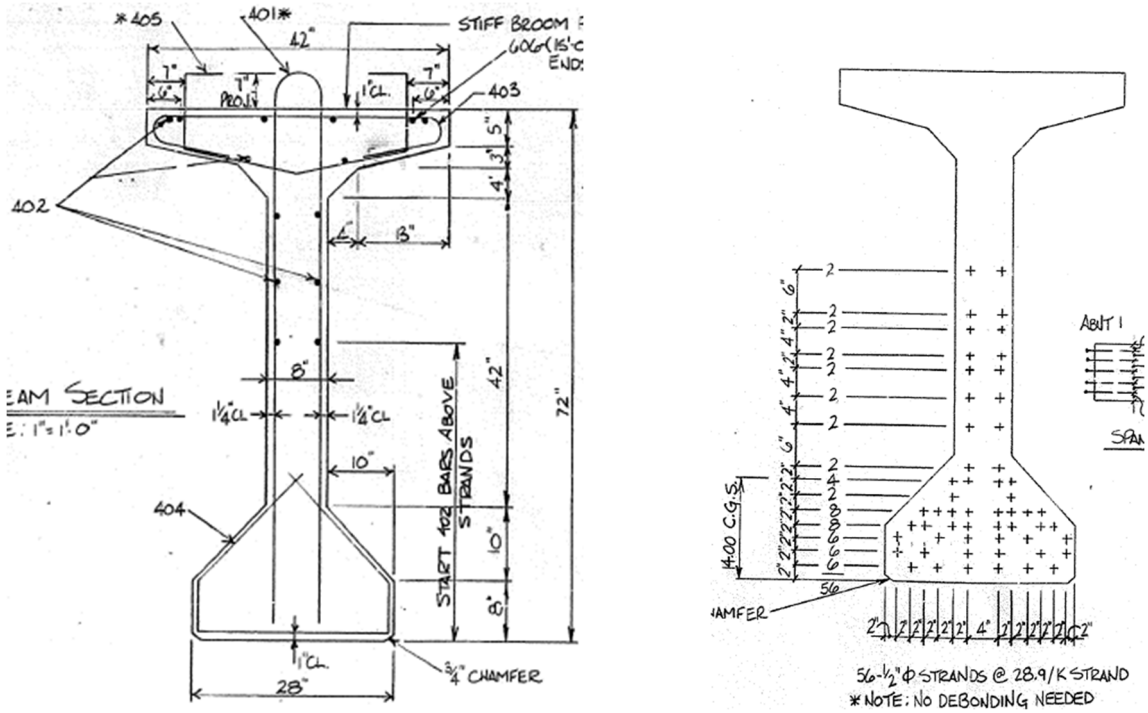

(a) Reinforcement arrangement (b) Strands arrangement

Figure 25: Cross-section of the PennDOT sample bridge girder in the targeted span

Table 2: Summary of gravity load for the PennDOT sample bridge girder

Dead load	Calculation	DL Per Girder	Unit
Deck Slab	(150pcf)(45.5ft)(9in)/12/4	1280	plf
Girder Self Weight		1133	plf
Barrier	2(150pcf)(330in^2)/144/4	172	plf
Haunch weight	(0.5in)(42in)/144(150pcf)	22	plf
Wearing surface	(25psf)(45.5ft)/4	284	plf
	Total DL per girder	2891	plf
Live load		LL Per Girder	Unit
Uniform Lane Load	(640plf/lane)(3 lanes)/4	480	plf
Load Combination		Load Per Girder	Unit
DL+0.3LL		3034.8	plf

Fire modeling approach

The Modified Discretized Solid Flame (MDSF) model [1] is used here to calculate the thermal impact result from a localized fire hazard. Generally, the MDSF model simulates the fire as a 3D object that emits heat flux to the potential structure members. Applying the MDSF model involves five steps: (1) select a stand-in hydrocarbon fuel type and calculated equivalent pool fire footprint size for the fire HRR; (2) calculate fire geometry, particularly the overall flame height and the layering of luminous flame and smoke zones; (3) assign emissive powers that correspond to each zone; (4) apply an appropriately small mesh discretization to the flame and smoke surfaces (which will require an initial sensitivity analysis); and (5) calculate the radiation heat transfer as a summation of contributions from each discretized surface per its individual emissive power and view factor to the target.

The flame height H_f for the MDSF model is calculated using Heskestad's correlation [27] (Eq. (1)), and the surfaces of the extruded 3D solid flame shape are discretized into radiation-emitting elements. Sizing of the surface element mesh should be determined via preliminary convergence analyses for the target standoffs of interest. Generally, the maximum discretized edge dimension can be taken as 1% of the footprint perimeter, resulting in approximately square elements with 0.3-m maximum dimension for a 10-m diameter circular fire. Each surface element i is assigned an emissive power, E_i (kW/m^2), based on its vertical location. As shown in Figure 26, the MDSF represents a gasoline or diesel pool fire (which, like most hydrocarbon fuels, have significant soot yield when burning [67]) as vertically divided into a luminous visible flame lower zone and a smoke-cone upper zone. The shape of the footprint could be either rectangular or circular, as needed.

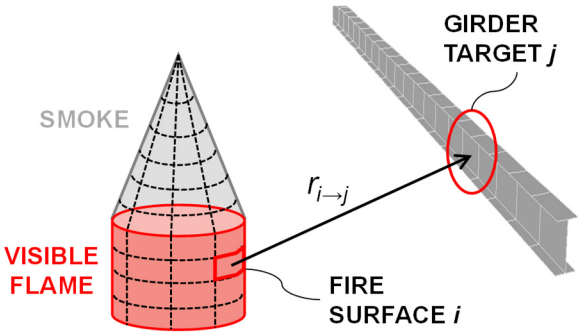

Figure 26: Illustrations of heat transfer from the MDSF model [1] of an open-air hydrocarbon pool fire to a discretized target

This model consists of two 3D objects that together are more representative of realistic pool fires [68–73]: a flame cylinder+cone (which is assigned a constant emissive power over its surface), and a smoke cylinder+cone "hat" which obscures the top portions of the flame shape. Based on previous work by Zhou et al. [74] and Shen et al. [75], the geometry of the flame shape in Figure 27b has a total height H_f per Eq. (1). Zhou et al. [74] proposed a constant value of $0.4H_f$ for the height of the cylinder based on the results laboratory-scale pool fire tests with heptane [76]. Shen et al. [75] utilized a semi-empirical expression that calculates the cylinder height relative to the pool fire diameter based on laboratory-scale tests with natural gas flames [77]. This height of the cylinder is set equal to the maximum luminous zone height based on experimental observations for the selected fuel. For example, previous experiments by Munoz et al. [68] indicated that for pool diameters less than 5m, the luminous zone is located below $0.45H_f$ for gasoline pool fires and $0.30H_f$ for diesel pool fires. Based on these observations, the value of φ_{cyl} in Figure 27b for gasoline and diesel is set equal to 0.45 and 0.30, respectively, for all pool diameters. More experiments are needed to determine φ_{cyl} values for other types of hydrocarbon fuel. In the absence of experimental data, the cylinder heights proposed by Zhou et al. [74] or Shen et al. [75] could be used as alternatives.

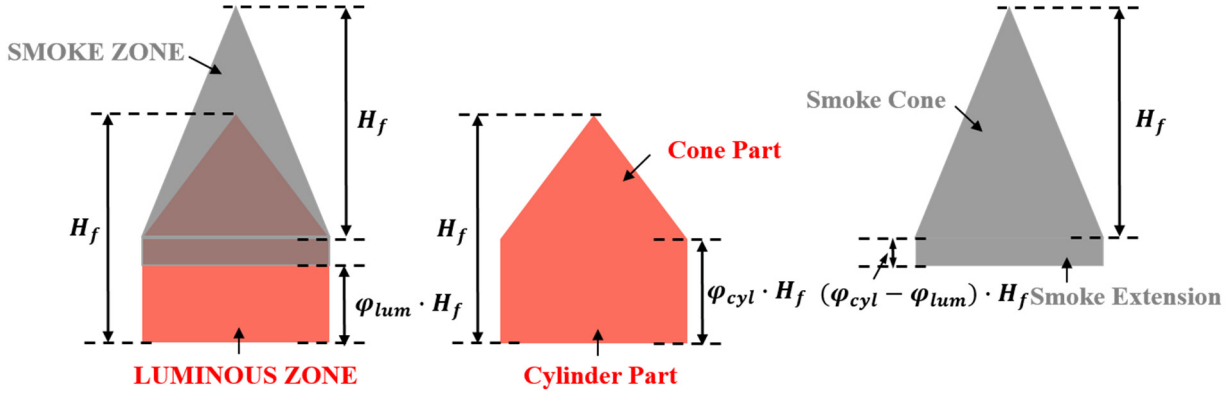

(a) Proposed MDSF model (b) Flame Shape (c) Smoke Hat

Figure 27: Flat elevation of the proposed MDSF model with a circular footprint (shown without mesh discretization for clarity) [2].

The smoke hat is positioned such that the base of its cone aligns with the base of the flame cone (at $\varphi_{cyl} \cdot H_f$) as shown in Figure 27a. The height of the smoke hat's cone is set equal to H_f to provide a good correlation with experimental data and FDS results. The smoke hat's cylinder extends downward from the base of its cone to obscure a portion of the flame cylinder, according to experimental observations. In Figure 27a, the ratio of luminous height to the total flame height is denoted as φ_{lum}, the value of which is a function of fuel type and pool diameter. The value of φ_{lum} is calculated using semi-empirical expressions per Munoz et al. [78], which are summarized in Table 3.

Table 3: Luminous ratio (φ_{lum}) of the MDSF model per [78]

Parameters		Gasoline	Diesel
φ_{lum}	$D_{f,eff} \leq$ 5m	0.45	0.30
	5m < $D_{f,eff} \leq$ 20m	$aD_{f,eff}^{b} - c$	$aD_{f,eff}^{b} - c$
	$D_{f,eff}$ > 20m	0.05	0.05
Constants	a	1.80	1.26
	b	-0.377	-0.257
	c	0.533	0.533

For pool fires with diameters less than 5m, $\varphi_{lum} = \varphi_{cyl}$ and the smoke cylinder's downward "extension" becomes negligible. As the pool diameter increases from 5m to 20m, the value of φ_{lum} decreases, and the smoke extends downward to obscure more of the flame cylinder [68,79]. At pool fire diameters greater than 20m, most of the flame shape is covered by smoke and φ_{lum} is equal to 0.05. Separate emissive powers are assigned to the flame and smoke portions of the MDSF model to represent the realistic distribution of radiative emission from hydrocarbon pool fires. Flame emissive power, E_{flame} (kW/m^2), is calculated as an emitted fraction of peak HRR and is uniformly applied to all discretized surfaces of the flame shape in Figure 27b:

$$E_{flame} = \frac{\chi_{r,f} \cdot \dot{Q}_{f,max}}{A_{f,M}} \tag{10}$$

where $\dot{Q}_{f,max}$ (kW) is the peak HRR; $A_{f,M}$ (m^2) is the total surface area of the flame shape; and $\chi_{r,f}$ is the radiative fraction of the flames. Semi-empirical expressions for the radiative fraction of the entire fire, χ_r, have been previously proposed by others [79–81] based on experimental measurements of radiant heat flux from a wide range of hydrocarbon pool fires. These χ_r expressions, such as that per McGrattan et al. [79], are typically a function of pool diameter and are often used for the point source model or solid flame model calculations that assume a single emissive power value for the entire fire. To calculate $\chi_{r,f}$, the McGrattan et al. expression is generalized to account for the radiative emissions from only the flame portion of the MDSF model:

$$\chi_{r,f} = \chi_{r,f_{max}} e^{-k \cdot D_{f,eff}} \tag{11}$$

values of $\chi_{r,f_{max}} = 0.37$ and $k = 0.025\text{m}^{-1}$ were selected by Zhu and Quiel [2] for open-air gasoline and diesel pool fires via calibration against experimental data and FDS results. Note that $\chi_{r,f}$ is only proposed for gasoline and diesel pool fires – application to other fuel types requires further investigation.

As shown in Figure 27, the smoke hat will obscure the upper portions of the MDSF model's flame shape above $\varphi_{lum} \cdot H_f$ and provide a lower emissive power. Figure 28 shows that the emissive power of the visible surfaces of the MDSF model is vertically divided into three regions:

1. At $0 < H < \varphi_{lum} \cdot H_f$, the emissive power of the unobscured luminous zone equals E_{flame} per Eqs. 14 and 15.
2. At $\varphi_{lum} \cdot H_f < H < \varphi_{cyl} \cdot H_f$, the emissive power in the smoke cylinder extension linearly transitions in the upward direction from E_{flame} to a maximum value of E_{smoke}. If $E_{flame} > E_{smoke}$, then $E_{smoke} = 40$ kW/m^2 per Munoz et al. [68]. If $E_{flame} < E_{smoke}$, then $E_{smoke} = E_{flame}$ as a limiting value, and the emissive power in this region is therefore constant.
3. At $\varphi_{cyl} \cdot H_f < H < (1+\varphi_{cyl}) \cdot H_f$, the emissive power in the smoke cone linearly decreases from E_{smoke} to zero as the smoke whirl cools with increasing vertical distance from the flames.

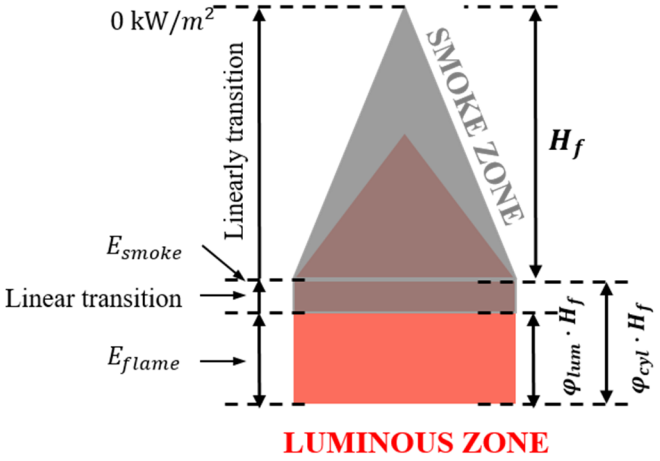

Figure 28: Emissive power distribution for the MDSF model (shown without mesh discretization for clarity) [2]

The total thermal radiation delivered to a target located outside the 3D fire shape is a summation of the contributions from all discretized surfaces that have a view of the target. The radiant heat flux from the MDSF model to target surface *j* is calculated via Eq. (12):

$$\dot{q}_j^{''} = \sum_{i=1}^{n} E_i F_{i \to j} = \sum_{i=1}^{n} E_i \frac{A_i cos\theta_i cos\theta_j}{\pi r_{i \to j}^m} \tag{12}$$

Here, the value of $m = 2.3$ was determined via calibration against the experimental data and CFD results.

Based on a preliminary convergence study, the MDSF models are meshed to have 100 elements around their circumference and 200 elements over the full height $[(1+\varphi_{cyl}) \cdot H_f]$ of the flame+smoke shape shown in Figure 28. The spacing of the vertical mesh is tailored to accommodate the transitions from the visible flame to the smoke zone

and from the cylinder to the cone. For this study, the MDSF model was programmed in Matlab [82] to calculate the summation of heat flux contributions from all discretized surfaces that have a view of the target.

For the case that fire locations are directly beneath a bridge, and a low clearance or consideration of an intense fire with large H_f may result in the MDSF geometry being interrupted by and thereby partially engulfing the bridge overhead. The MDSF model can be conservatively adapted to this scenario, as shown in Figure 29. When the smoke cone is interrupted by the bridge deck, its shape is warped into an inverted truncated cone that spans vertically from the lower edge of the smoke layer up to the bridge deck. The new interrupted shape has the same volume as the original cone, thus ensuring the conservation of mass via soot production and setting a radius for smoke spread underneath the bridge deck. E_{smoke} is still set to 40 kW/m^2 at the base of the inverted truncated cone and has the same linear decrease over the height of the original cone – E_{smoke} at the top of the new shape, therefore, has an interpolated value defined by its vertical distance above the base of the original smoke cone. The emissive power for the flame is calculated via Eq. (10). Note that as the flame is interrupted, as shown in Figure 29, the flame surface area ($A_{f,M}$) decreases, thus increasing E_{flame}.

Targets located outside the smoke layer (Region 1 in Figure 29) receive heat flux from the smoke and flame surfaces per Eq. (12) in the same way as the original MDSF model, which assumes that the smoke obscures the flame surfaces underneath. Targets that are engulfed by the new smoke shape (Region 2) receive a direct flux (accounting for convective effects) from the smoke at a value equal to the interpolated E_{smoke} at the top edge. Since they are within the turbulent smoke layer, these targets can also see the flame surfaces on the flame cone and receive their associated radiation heat flux. For targets engulfed by the flame cone (Region 3), $\dot{q}_j^{''}$ is set equal to the lesser of E_{flame} per Eq. (10) and an empirical engulfed-in-flame direct heat flux of 170 kW/m^2. The engulfed value conservatively combines direct flame radiation and convective heat transfer into a single heat flux that is based on experimental measurements of objects engulfed in a hydrocarbon fire. If the girders are engulfed by the flame cylinder at a location below the smoke layer, then smoke effects are neglected, and all girders within the flame cylinder receive the full engulfed-in-flame heat flux.

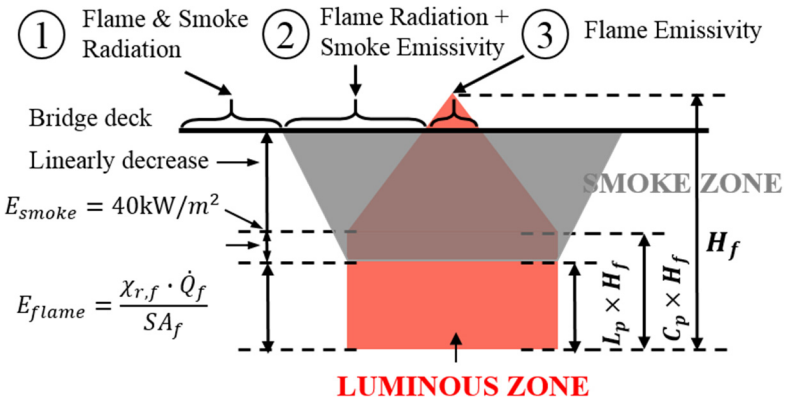

Figure 29: MDSF model showing the smoke zone without bridge deck interruption [14].

Fire scenario selection

Preliminary fire scenario: Hay bales stored under the bridge

The sample bridge is evaluated for a range of potential fire hazards. The first concern raised by PennDOT is the presence of hay bales under the bridge. This is a likely occurrence in rural Pennsylvania where state bridges cross private farm-land as shown in Figure 30a. In this scenario, the combustible material is the hay bale stack. From the picture, there are seven layers of hay bales stacked together. The assumption is made that a bale of hay has typical size of 36 in. (length) × 18 in. (width) × 16 in. (height), and weights 18 to 27 kg, the distance from the bottom of the girder to the top of the bales, at the lower 15 ft vertical clearance condition, is 5.7 ft. As a conservative assumption the hay bales are placed at midspan in the area framed by the red rectangular box, as shown in Figure 30b. The bales are assumed to transversely cover the bridge width, and longitudinally half the value of the bridge width. The stack is assumed to be seven bales high, resulting in a distance of 5.7 ft from the top surface of the hay bales to the bottom of the PS girders.

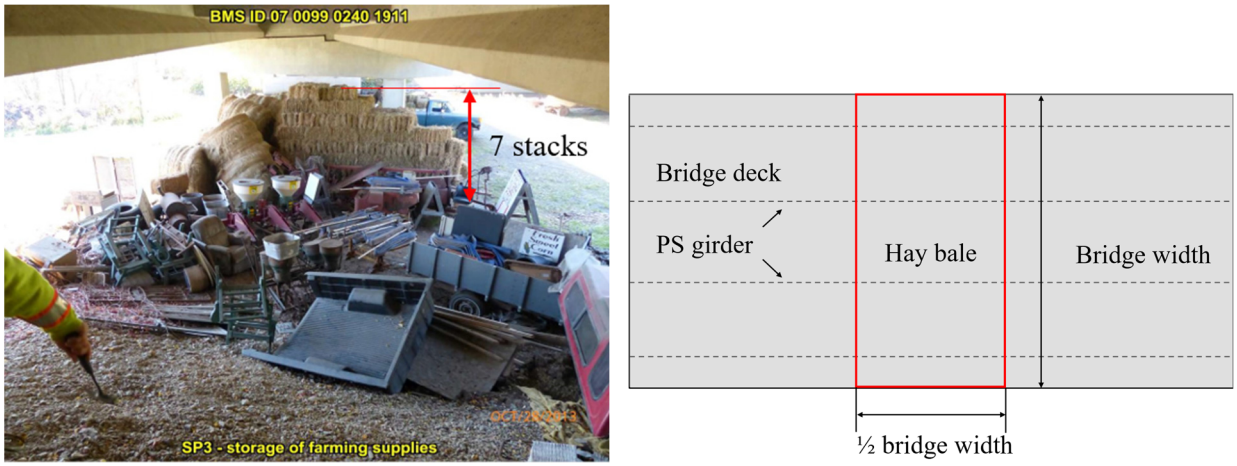

(a) Cargo stored underneath the bridge

(b) Arrangement of the hay bale

Figure 30: Hay bale fire load stored underneath the PennDOT sample PS concrete bridge

The combustion properties of straw as fuel are presented in Table 4. The value of heat of combustion from various references is consistent and ranges from 10 to 18 MJ/kg. This study used the value of 15.6 MJ/kg, which is provided by the SFPE handbook [26], for the subsequent calculation. The data source for heat release rate is rare. This study takes a conservative value of 180 kW/m^2 to calculate the geometry properties (i.e., flame height) of the fire. Compared to the hydrocarbon pool fire, this fire has a much lower energy density and is thus much milder. Together with the region for hay bale storage, as shown in Figure 30b, the HRR is 16.1 MW. For the footprint area shown in Figure 30b, this HRR yields a flame height of 0.4 m per Eq. (1), which is smaller than the distance from the top of the hay bale to the bottom of the girder. Applying the MDSF fire model, which will be introduced in the next section, for thermal impact calculation, the distribution of the heat flux on the PS girders is presented in Figure 31. As shown, even with a large amount of hay bales at a very low standoff the maximum heat flux is only 20 kW/m.^{2} This low thermal demand will not likely result in structural problems for the bridge based on preliminary studies. To examine the system more comprehensively additional thermal demands are investigated. Specifically, vehicle fire hazards are introduced to investigate the thermo-structural vulnerability of this prototype system

Table 4: Combustion properties of straw

Reference	Heat of Combustion (MJ/kg)	Peak HRR (kW/m^2)
SFPE handbook [26]	15.6	-
Fire hazard of compressed straw as an insulation material for wooden structures [83]	11.6	171.42
Characterization of burning behaviors and particulate matter emissions crop straws based on a cone calorimeter [84]	13.82-15.48	104-167
Solid fuel production from straw [85]	18 (or 43000 kcal/kg)	-
HRR characterization of NFPA 1403 compliant training fuels [86]	12.4-15.7	-
Buchanan and Abu [87]	20	-

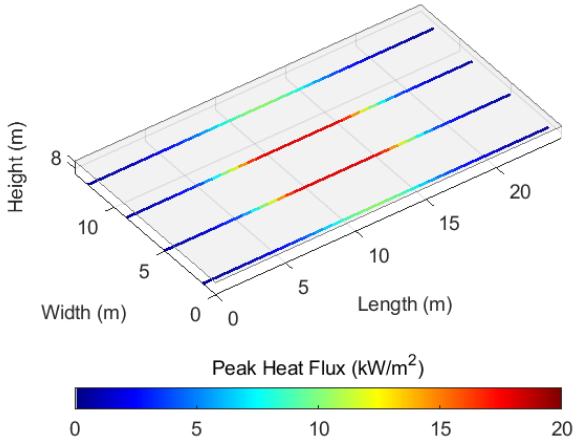

Figure 31: Heat flux distribution of the PS girders subjected to the hay bale fire

Vehicle fire intensity

Chapter 7 of NFPA 502 [6] provides HRR values for several classes of vehicle fires in tunnels, as summarized in Table 5, which could be used as a reference for bridge fire analysis. These vehicle classes range from single passenger cars up to heavy goods vehicles (HGVs, which can carry a wide assortment of potential fuels) and tanker trucks carrying flammable liquids. This study selects the bus fire (30 MW), HGV fire (150 MW), and a fire intensity in between (70 MW, representing a smaller HGV) as the sample fire hazards to investigate the vulnerability of the sample PS concrete girder bridge.

Table 5: Peak heat release rates (HRR) for design fires in tunnels per Chapter 7 of the 2017 edition of NFPA 502 [6]

Vehicles	Experimental HRR		Representative	
	Peak HRR (MW)	Time to Peak HRR (min)	Peak HRR (MW)	Time to Peak HRR (min)
Passenger car	5-10	0-54	8	10
Multiple passenger cars	10-20	10-55	15	20
Bus	25-34	7-14	30	15
Heavy goods truck	20-200	7-18	150	15
Flammable/combustion liquid tanker	200-300	-	300	-

The total combustion energy E_{tot} (GJ) for vehicle fires could be calculated as a function of the peak HRR. The data used by Ingason [88] of a set of large-scale vehicle fire experiments could be used to generate an "upper bound" regression (E_{tot}^{up}, plotted red in Figure 32), while experimental data collated by Guo et al. [89] was used to develop a "lower bound" regression (E_{tot}^{low}, plotted blue in Figure 32). This study uses the upper bound combustion energy for conservative evaluation.

$$E_{tot}^{up} = 3.31\dot{Q}_{max}^{1.066} \tag{13a}$$

$$E_{tot}^{low} = 16.47e^{0.01257\dot{Q}_{max}} \tag{13b}$$

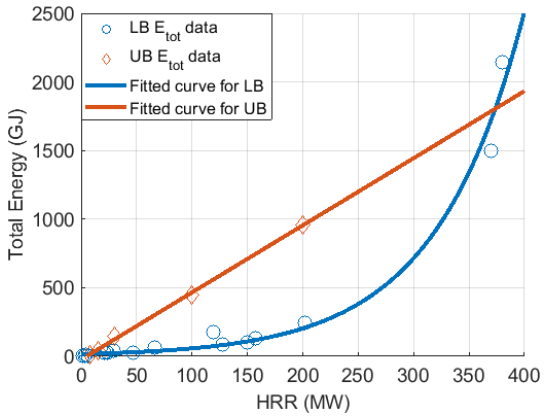

Figure 32: Estimated total combustion energy of vehicle fires with respect to HRR

The time history of heat release from the vehicle fire can be calculated following the quadratic curve proposed by Ingason [88]. It consists of a quadratic growth from zero to time t_{max}(min), a constant peak HRR ($\dot{Q}_{f,max}$) value to the time t_D(min), and an exponential decrease from the peak HRR value to zero. If $t_D \leq t_{max}$, then no constant peak HRR period is obtained.

$$\begin{aligned} &for\ 0 \leq t_{max}: && \dot{Q}_f(t) = \alpha_{g,q} t^2 \\ &for\ t_{max} < t < t_D: && \dot{Q}_f(t) = \dot{Q}_{f,max} \\ &for\ t \geq t_D: && \dot{Q}_f(t) = \dot{Q}_{f,max} e^{-\alpha_{D,q}(t-t_D)} \end{aligned} \quad (14)$$

$$t_{max} = \sqrt{\dot{Q}_{f,max}/\alpha_{g,q}} \quad (15)$$

$$t_D = \frac{\chi E_{tot}}{\dot{Q}_{f,max}} + \frac{2}{3} t_{max} - \frac{1}{\alpha_{D,q}} \quad (16)$$

where χ is the combustion efficiency (set to 1 for conservative estimation of the constant maximum HRR period; and E_{tot} is the total calorific value of the fuel (MJ) that could take the upper bound value E_{tot}^{up}. The values of $\alpha_{g,q}$ (kW/s^2) and $\alpha_{D,q}$ (-/s) vary with respect to the type of vehicles and are summarized in Table 6.

Table 6: Design parameters for the creation of design fire for traffic vehicles

Type of vehicle	$\dot{Q}_{f,max}$ (MW)	$\alpha_{g,q}$ (kW/s^2)	$\alpha_{D,q}$ (/s)
Car	4	0.01	0.001
Bus	30	0.1	0.0007
Truck	15-130	-	-
Train	15	0.01	0.001
Subway car	35	0.3	0.001

The three fire scenarios are placed underneath the PennDOT sample bridge at different locations. Vertically, their bases are located at 15 ft, 30 ft, and 45 ft clearance, which is measured from the bottom of the PS girders. Longitudinally, the midspan and quarter span are selected for flexural evaluation. The distribution of peak heat flux on the PS girder as subjected to the fire hazard at the middle span are presented in Figure 33. As illustrated, the 150 MW fire at 15 ft clearance engulfs a large portion of the PS concrete girder and produced a significant thermal impact. The heat flux distribution from the 70 MW fire at 15 ft resembles the case of 150 MW fire at 30 ft and is omitted from

the subsequent structural analysis. Similarly, the 30 MW fire at 30 ft clearance is not conducted since its heat flux distribution is similar to the case of the 70 MW fire at 45 ft clearance. The case of the 30 MW fire at 45 ft is omitted since the peak heat flux is too low to cause any damage to the PS girder. The fire scenarios for analysis are framed with red dash boxes. An additional study is conducted on these chosen fire size and standoffs with the fire located at the ¾ span. Prior to performing the analyses for specific vehicle fires, the bridge system is analyzed for a worse-case scenario where the entire PS girder is exposed to the ASTM E1529 fire curve.

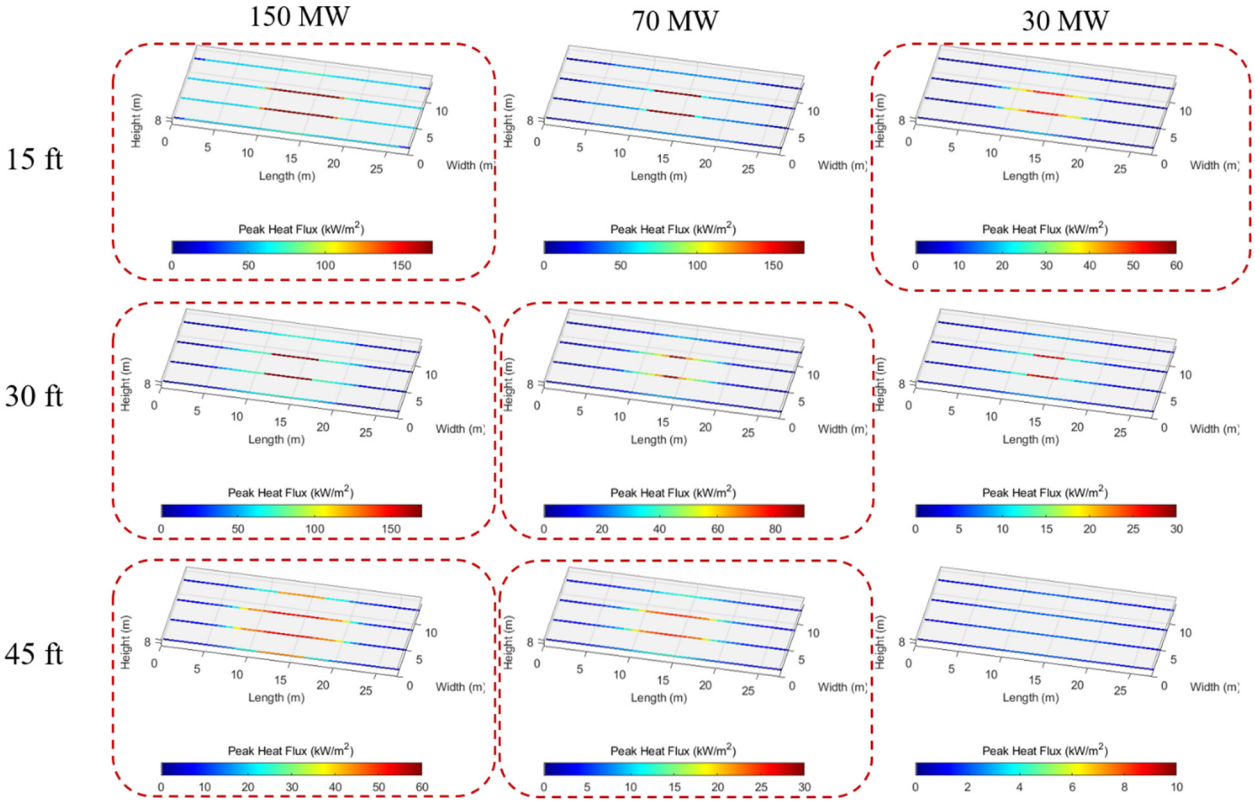

Figure 33: Heat flux distribution on girders subjected to fires of various magnitude and clearance

Thermo-structural analysis

The thermo-structural analyses follow the procedure applied to the I-85 highway interchange as introduced in this report, and the damage states of the entire bridge are classified. To improve computational efficiency, the 91-ft sample bridge is divided into 30 elements; each element has an approximate length of 3 ft.

Damage classification

The structural response modeling results are used to develop damage descriptions for the bridge as a whole. Damage is described using maximum and residual displacement for the PS concrete girder bridge. The damage levels used in this study are as follows (where *L* is the length of the span between piers):

- **SUPERFICIAL**: Maximum residual deflection is less than *L/800* (based on the AASHTO 2014[4] serviceability limit). Also, the maximum deflection during the fire is less than *L/200* (i.e., 10x the critical deflection limit of *L/20* [7]). A small amount of permanent deformation has occurred, potentially requiring small amounts of repair but remaining reusable.
- **MODERATE**: Maximum residual deflection is less than *L/200* (i.e., 4x the AASHTO serviceability limit), while the maximum deflection during the fire is less than *L/100*. A larger amount of permanent deformation has occurred, requiring an increasingly significant amount of repair and possible replacement.
- **HEAVY**: Maximum residual deflection is less than *L/100* (i.e., 8x the AASHTO serviceability limit), while the maximum deflection during the fire is less than *L/20.* Post-fire replacement will most likely be required.
- **HAZARDOUS**: Maximum deflection during the fire is larger than *L/20*. The probability of collapse has significantly increased. Replacement will be required.

In practice, these damage levels can be tailored to any set of design objectives or damage thresholds in accordance with owner requirements, modeling capabilities, or other constraints.

Results

Figure 34a presents the displacement of the middle span of the sample PS girder subjected to the ASTM E1529 fire curve, as presented in Figure 6. The bold red solid line represents the case where heating continues until the bridge fails. It can be observed that the failure time of the PennDOT sample bridge is 172 minutes, which is much longer than the failure time of span 30NB in the fire hazard in 2017 (76 mins), though they share the consistent span length, load combination, and thermal loading. From the deformed shape (amplified by ten times) at the time of the collapse, as presented shown in Figure 34b, there is no "kink" in the PennDOT system. As noted previously the I-85 bridge formed a localized high region of rotation along the span under thermal exposure. The reason for the improved performance can be mainly attributed to the use of straight strands in the PennDOT section. This keeps all the strands in the bottom bulb providing thermal protection, unlike the I-85 where the deflected strands were located in the thin web and were subject to high thermal demands. At the time of the collapse, the moment capacity of the middle span elements decreases to the demand level, as presented in Figure 35a.

The shear failure is also checked per Figure 35b for the cross-section at the support due to ASTM E1529 fire exposure along the full length of the girder. The results indicate that the aggregate shear capacity from the concrete, vertical mild steel, and PS strands diminishes due to heating and begins to converge toward the applied shear just after 150 minutes. The shear capacity is therefore reached just slightly before the onset of flexural runaway at 172 minutes; however, the applied shear plotted in Figure 35b is taken at the very end of the girder. the effective shear at an end-offset equal to the depth of the girder would be slightly less, and that value would not be reached sooner than the time of flexural runaway at 172 minutes. Though shear response is more critical for the PennDOT girder section (with straight strands) than for the I-85 girder section (with harped strands), flexural runaway is still considered to be the primary mode of failure for the PennDOT girder when exposed to the ASTM E1529 fire.

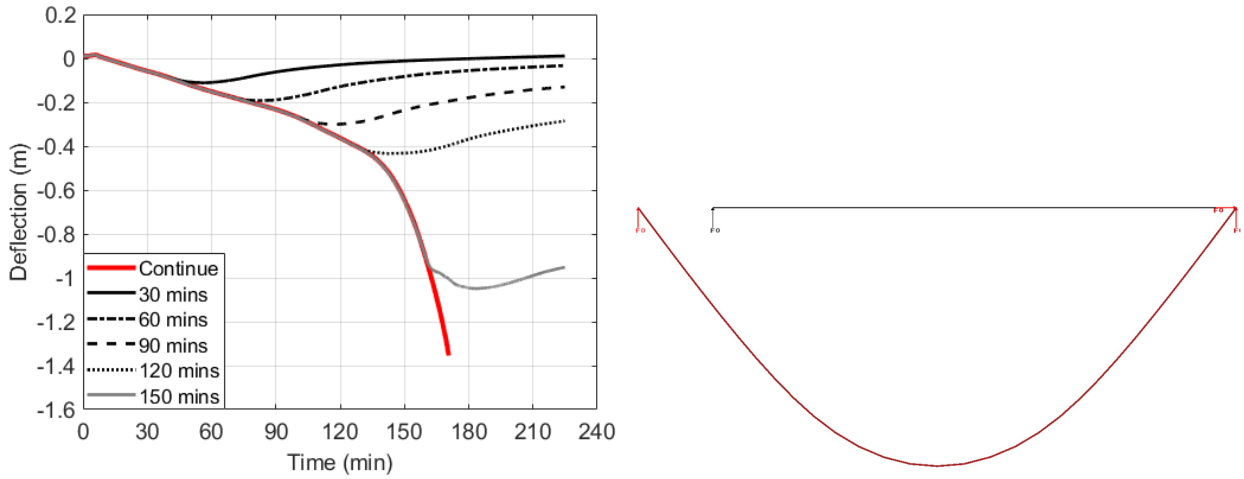

(a) Displacement time history of the middle span (b) Deformed shape at the time of collapse (x10)

Figure 34: Displacement of the middle span of the sample PS girder subjected to ASTM E1529 fire curve

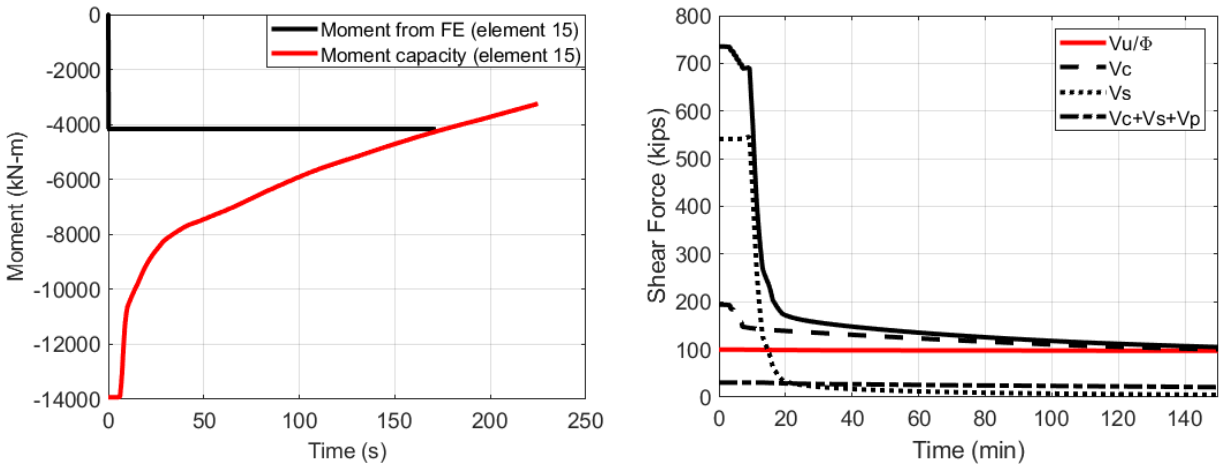

(a) Moment at middle span (b) Shear at support

Figure 35: Capacity vs. demand for sample bridge girder

To comprehensively assess the sensitivity to fire induced damage, the fire exposure is halted at varying time intervals: 30, 60, 90, 120, and 150 min. Applying the damage categorization introduced previously, the bridge vulnerability to fire hazards can be developed. For example, per Figure 34a, the PS girder subjected to 120 mins of ASTM E1529 heating reaches heavy damage since the maximum displacement is 0.42 m (<*L*/20 and >*L*/100) and the residual displacement 0.25 m (<*L*/100 and >*L*/200). Similarly, the 60 min heating time results in moderate damage as the maximum displacement is 0.20 m (<*L*/100 and >*L*/200) and the residual displacement is 0.05m (<*L*/200 and >*L*/800). The comprehensive results are listed in Table 7.

The deflection time histories of the sample bridge girder subjected to vehicle fire scenarios selected for analyses per Figure 33 are presented in Figure 37 through Figure 42. For the case that the fire is placed in the middle span, the maximum deflection is at node 31 of element 15. For the case that the fire is at quarter span, node 39 of element 19 has the largest deflection, as shown in Figure 36.

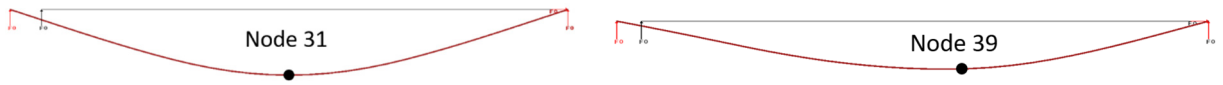

(a) Fire at midspan (b) Fire at quarter span

Figure 36: Location of the maximum deflection

The damage level resulting from each fire scenario is summarized in Table 7. Some conclusions can be made based on the observation of these figures. First, when straight strands are used in the PS concrete girder, the fire at midspan results in larger deflection and residual displacement. Second, though the failure time and maximum defection for 150 MW at 15 ft and 30 ft are similar, the latter one has less residual deflection for scenarios when the fire burns out before flexural failure is reached. Third, in the case that the fire is placed at the quarter span, the residual deflection is much smaller than in the case that the fire is located at the midspan. According to the results presented in Table 7, more heating time results in a higher level of damage. Specifically, a fire duration longer than 60 mins has the possibility to cause heavy damage to the bridge, while the hazardous damage may occur after 2 ½ hours of fire exposure.

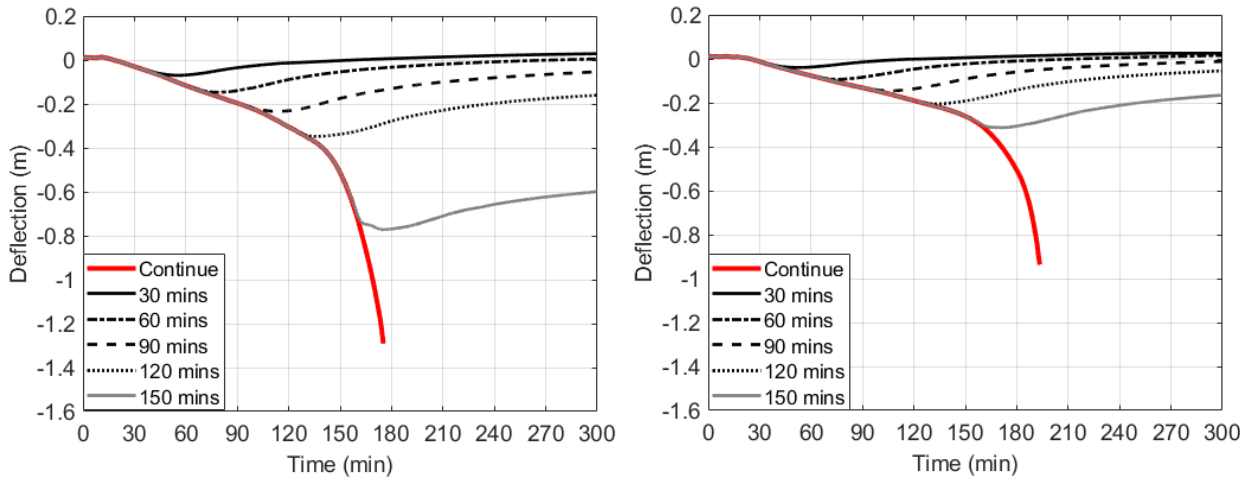

(a) At midspan

(b) At quarter span

Figure 37: 150 MW fire at clearance of 15 ft

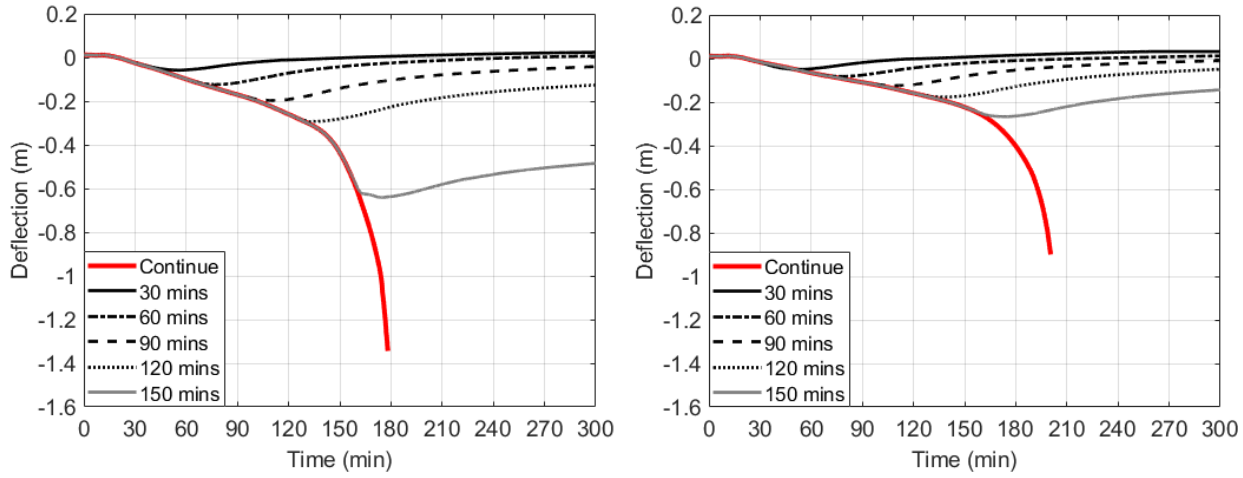

(a) At midspan

(b) At quarter span

Figure 38: 150 MW fire at clearance of 30 ft

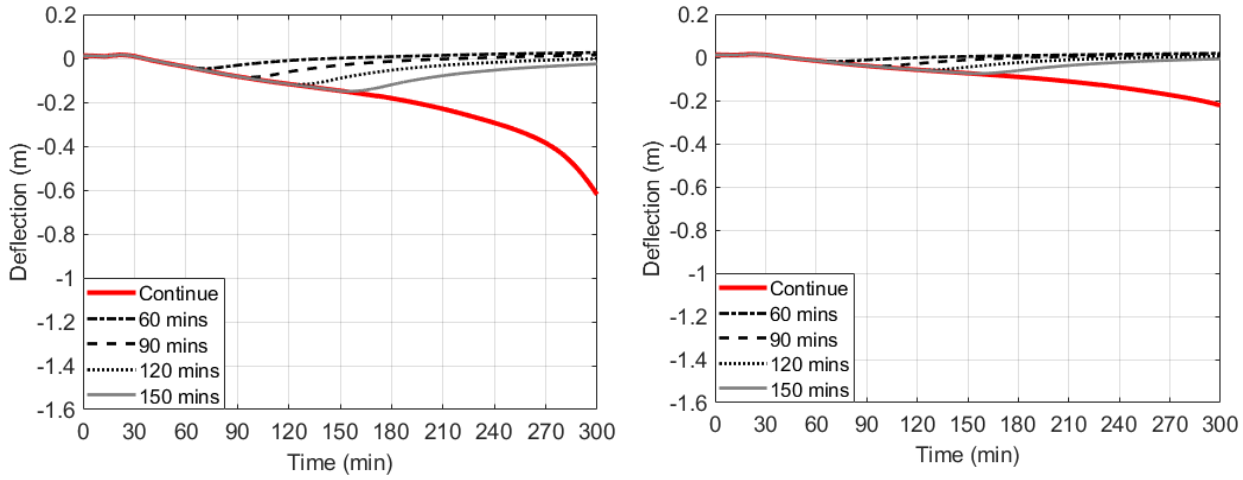

(a) At midspan

(b) At quarter span

Figure 39: 150 MW fire at clearance of 45 ft

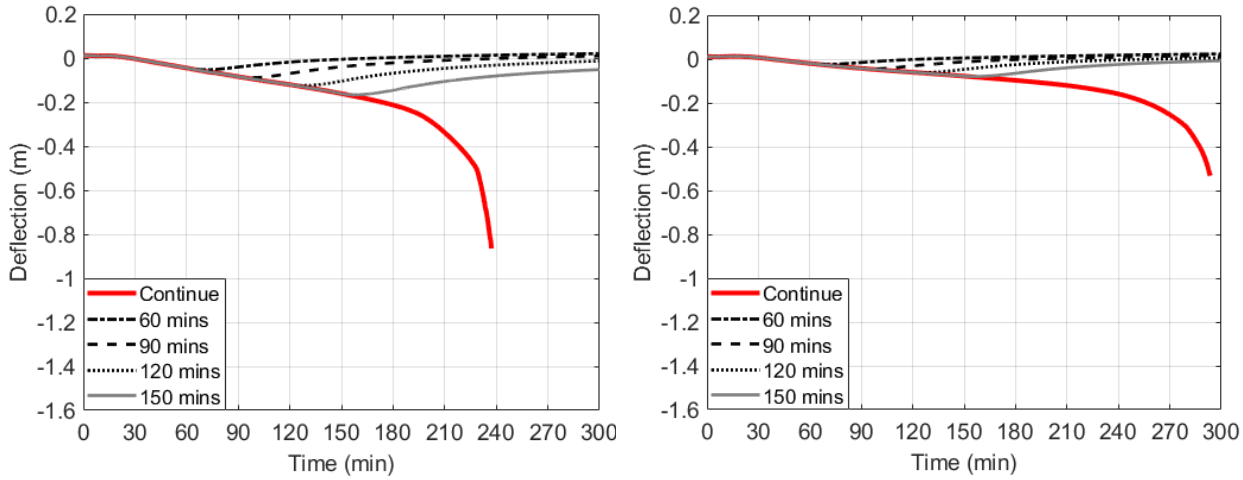

(a) At midspan

(b) At quarter span

Figure 40: 70 MW fire at clearance of 30 ft

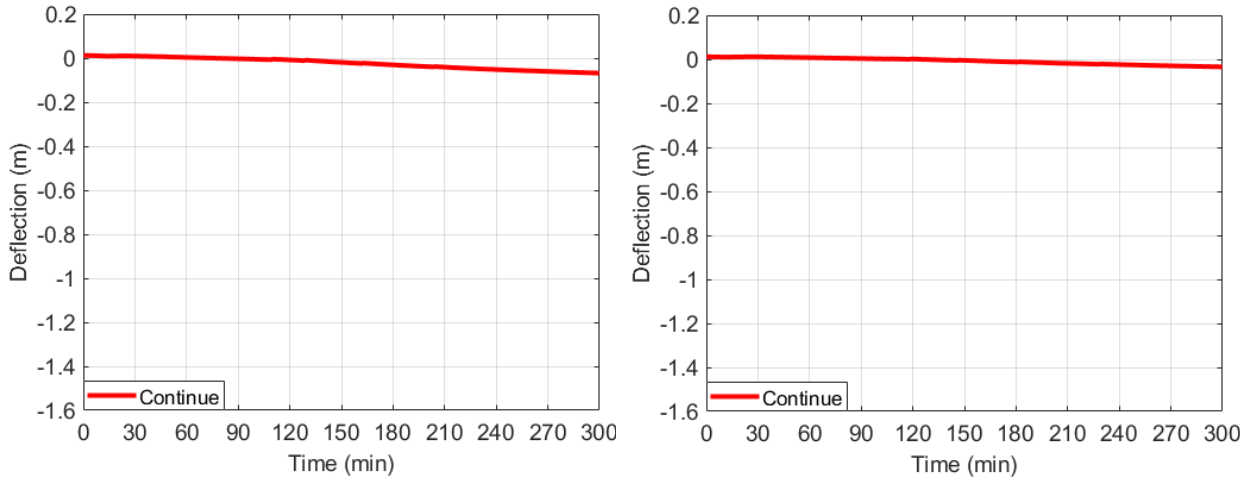

(a) At midspan (b) At quarter span

Figure 41: 70 MW fire at clearance of 45 ft

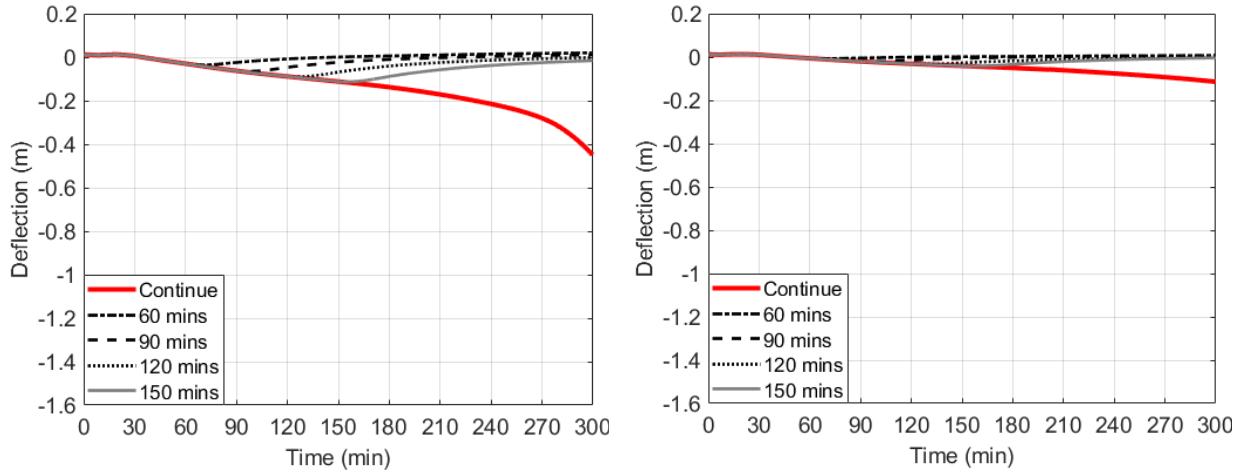

(a) At midspan (b) At quarter span

Figure 42: 30 MW fire at clearance of 15 ft

Table 7: Summary of deflections (m) and damage levels for the PennDOT PS girder subjected to various vehicle fire scenarios.

Fire Scenario		Heating location	Heating Duration								
			Continue			30min			60min		
			Max	Residual	Time to failure	Max	Residual	Damage	Max	Residual	Damage
ASTM E1529		full span	1.35	N/A	172 mins	0.12	0	Superficial	0.2	0.03	Moderate
150 MW	15 ft	midspan	1.35	N/A	175 mins	0.08	0	Superficial	0.15	0	Moderate
		quarter span	0.96	N/A	192 mins	0.03	0	Superficial	0.1	0	Superficial
	30 ft	midspan	1.35	N/A	179 mins	0.025	0	Superficial	0.124	0	Superficial
		quarter span	0.9	N/A	202 mins	0.016	0	Superficial	0.08	0	Superficial
	45 ft	midspan	0.62	N/A	N/A	~0	0	Superficial	0.02	0	Superficial
		quarter span	0.21	N/A	N/A	~0	0	Superficial	~0	0	Superficial
70 MW	30 ft	midspan	0.85	N/A	238 mins	~0	0	Superficial	0.03	0	Superficial
		quarter span	0.55	N/A	N/A	~0	0	Superficial	~0	0	Superficial
	45 ft	midspan	0.03	N/A	N/A	Superficial					
		quarter span	0.01	N/A	N/A	Superficial					
30 MW	15 ft	midspan	0.43	N/A	N/A	~0	0	Superficial	0.02	0	Superficial
		quarter span	0.11	N/A	N/A	~0	0	Superficial	~0	0	Superficial
Thresholds for max displacement			*L/200=0.1385; L/100=0.277; L/40=0.629; L/20=1.385*								
Thresholds for residual displacement			*L/800=0.034; L/200=0.1385; L/100=0.277*								

Damage Key:

SUPERFICIAL: Maximum residual deflection is less than *L/800* (based on the AASHTO 2014 [4] serviceability limit). Also, the maximum deflection during the fire is less than *L/200* (i.e., 10x the critical deflection limit of *L/20* [7]). A small amount of permanent deformation has occurred, potentially requiring small amounts of repair but remaining reusable.

MODERATE: Maximum residual deflection is less than *L/200* (i.e., 4x the AASHTO serviceability limit), while the maximum deflection during the fire is less than *L/100*. A larger amount of permanent deformation has occurred, requiring an increasingly significant amount of repair and possible replacement.

HEAVY: Maximum residual deflection is less than *L/100* (i.e., 8x the AASHTO serviceability limit), while the maximum deflection during the fire is less than *L/20*. Post-fire replacement will most likely be required.

HAZARDOUS: Maximum deflection during the fire is larger than *L/20*. The probability of collapse has significantly increased. Replacement will be required.

Table 7 (continue): Summary of deflections (m) and damage levels for the PennDOT PS girder subjected to various vehicle fire scenarios.

Fire Scenario		Heating location	Heating Duration								
			90min			120min			150min		
			Max	Residual	Damage	Max	Residual	Damage	Max	Residual	Damage
ASTM E1529		full span	0.3	0.13	Heavy	0.42	0.27	Heavy	1.03	0.9	Hazardous
150 MW	15ft	midspan	0.22	0.08	Moderate	0.36	0.18	Heavy	0.78	0.6	Hazardous
		quarter span	0.16	0.04	Moderate	0.2	0.07	Moderate	0.3	0.18	Heavy
	30ft	midspan	0.2	0.05	Moderate	0.29	0.126	Heavy	0.62	0.48	Hazardous
		quarter span	0.12	0.01	Superficial	0.19	0.08	Moderate	0.266	0.17	Heavy
	45ft	midspan	0.08	0	Superficial	0.13	0.02	Superficial	0.17	0.03	Moderate
		quarter span	0.02	0	Superficial	0.04	0	Superficial	0.08	0	Superficial
70 MW	30ft	midspan	0.08	0	Superficial	0.13	0.02	Superficial	0.18	0.04	Moderate
		quarter span	0.03	0	Superficial	0.05	0	Superficial	0.08	0	Superficial
	45ft	midspan					Superficial				
		quarter span					Superficial				
30 MW	15ft	midspan	0.04	0	Superficial	0.09	0	Superficial	0.11	0.01	Superficial
		quarter span	~0	0	Superficial	0.03	0	Superficial	0.05	0	Superficial
Thresholds for max displacement			*L/200=0.1385; L/100=0.277; L/40=0.629; L/20=1.385*								
Thresholds for residual displacement			*L/800=0.034; L/200=0.1385; L/100=0.277*								

Damage Key:

SUPERFICIAL: Maximum residual deflection is less than *L/800* (based on the AASHTO 2014 [4] serviceability limit). Also, the maximum deflection during the fire is less than *L/200* (i.e., 10x the critical deflection limit of *L/20* [7]). A small amount of permanent deformation has occurred, potentially requiring small amounts of repair but remaining reusable.

MODERATE: Maximum residual deflection is less than *L/200* (i.e., 4x the AASHTO serviceability limit), while the maximum deflection during the fire is less than *L/100*. A larger amount of permanent deformation has occurred, requiring an increasingly significant amount of repair and possible replacement.

HEAVY: Maximum residual deflection is less than *L/100* (i.e., 8x the AASHTO serviceability limit), while the maximum deflection during the fire is less than *L/20*. Post-fire replacement will most likely be required.

HAZARDOUS: Maximum deflection during the fire is larger than *L/20*. The probability of collapse has significantly increased. Replacement will be required.

CONCLUSIONS

This study demonstrates a numerical simulation approach to investigate the thermo-structural response of the prestressed bulb-T concrete bridge girders subjected to fire hazards underneath. The approach is first used to analyze span 30NB of the I-85 bridge that collapsed due to severe fire in 2017 Atlanta. The results of this analysis showed good agreement with the outcomes of the actual event. Then, the proposed approach is applied to the PennDOT sample PS bridge girder to study its thermo-structural vulnerability. Several conclusions can be made from the results of these analyses:

- The failure mode of the span 30NB of the I-85 highway overpass in Atlanta in the fire hazard in 2017 was indicated to be the flexure runaway. The simulation introduced in this report successfully captured the failure time and failure location for that bridge fire event.
- The harped strands in the I-85 PS girder's web introduced a vulnerable thermo-structural flexural location away from midspan, which should be taken into account when conducting structural-fire evaluation. Considering the effects of thermally induced concrete spalling, the temperature of strands in the thinner web increased significantly, which reduces their yield strength. The harped strand increases the possibility of flexure failure but helps to strengthen the shear capacity.
- The moment capacity calculation procedure introduced in this study can effectively capture thermally induced reductions when exposed to fire hazards.
- The temperature-dependent shear capacity can be calculated from the results of 2D fiber element thermal analysis of the bulb-T cross-section by applying the corresponding strength reduction factors to the AASHTO LRFD specification. Shear capacity is significantly decreased due to the 2017 fire hazard for span 30NB, but shear failure is not the primary mode for this event.
- The sample bridge girder provided by PennDOT is more fire resistant than the I-85 bridge girder though they share consistent span length and load combination. This can be attributed to the following factors: (1) larger girder cross-section that mitigates the temperature increase of the embedded strands; (2) the use of straight strands, which keeps more of the reinforcement in the bottom bulb (with more concrete embedment) rather than in the thinner web; and (3) the presence of more strands, which reduces the percentage of the capacity that is affected by the thermal impact after the same time of exposure.
- As expected, longer heating times prior to fire burnout result in a higher level of damage. For the PennDOT sample bridge, fire durations longer than 60 minutes can cause heavy damage to the bridge, while hazardous damage may occur after 2 ½ hours of heating.
- In the case that the fire is placed at the quarter span, the residual deflection is much smaller than in the case where the fire is located at the midspan.

REFERENCES

[1] S.E. Quiel, T. Yokoyama, L.S. Bregman, K.A. Mueller, S.M. Marjanishvili, A streamlined framework for calculating the response of steel-supported bridges to open-air tanker truck fires, Fire Safety Journal. 73 (2015) 63–75. https://doi.org/10.1016/j.firesaf.2015.03.004.

[2] Z. Zhu, S.E. Quiel, Near-Field Radiant Heat Flux from Open-Air Gasoline and Diesel Pool Fires: Modified Point Source and Discretized Solid Flame Models, Fire Technol. (2021). https://doi.org/10.1007/s10694-021-01097-y.

[3] A. Carlton, Q. Guo, S. Ma, S.E. Quiel, C.J. Naito, Experimental assessment of explosive spalling in normal weight concrete panels under high intensity thermal exposure, Fire Safety Journal. 134 (2022) 103677. https://doi.org/10.1016/j.firesaf.2022.103677.

[4] AASHTO (American Association of State Highway and Transportation Officials), AASHTO LRFD Bridge Design Specifications, Seventh edition with 2016 interim revisions. Washington, D.C. : AASHTO, 2016.

[5] NTSB, NTSB/HAB-18/02: Fire Damage to Bridge and Subsequent Collapse, Atlanta, Georgia, National Transportation Safety Board, Washington, D.C., 2017. https://www.ntsb.gov/investigations/AccidentReports/Reports/HAB1802.pdf.

[6] NFPA, NFPA 502: Standard for road tunnels, bridges, and other limited access highways, National Fire Protection Association, Quincy, MA, 2017.

[7] I. Payá-Zaforteza, M.E.M. Garlock, A numerical investigation on the fire response of a steel girder bridge, Journal of Constructional Steel Research. 75 (2012) 93–103. https://doi.org/10.1016/j.jcsr.2012.03.012.

[8] G.C. Lee, S.B. Mohan, C. Huang, B.N. Fard, Technical Report MCEER-13-0008: A Study of U.S. Bridge Failures (1980-2012), MCEER, University at Buffalo, State University of New York, Buffalo, NY, 2013.

[9] M. Garlock, I. Paya-Zaforteza, V. Kodur, L. Gu, Fire hazard in bridges: Review, assessment and repair strategies, Engineering Structures. 35 (2012) 89–98.

[10] K. Wardhana, F.C. Hadipriono, Analysis of Recent Bridge Failures in the United States, J. Perform. Constr. Facil. 17 (2003) 144–150. https://doi.org/10.1061/(ASCE)0887-3828(2003)17:3(144).

[11] Z. Zhu, S.E. Quiel, A. Carlton, K.A. Mueller, S.M. Marjanishvili, Performance-based prioritisation of fire protection for steel girder overpasses in a complex highway interchange, Structure and Infrastructure Engineering. 16 (2020) 394–411. https://doi.org/10.1080/15732479.2019.1666884.

[12] J. Alos-Moya, I. Paya-Zaforteza, A. Hospitaler, P. Rinaudo, Valencia bridge fire tests: Experimental study of a composite bridge under fire, Journal of Constructional Steel Research. 138 (2017) 538–554. https://doi.org/10.1016/j.jcsr.2017.08.008.

[13] E. Aziz, V. Kodur, An approach for evaluating the residual strength of fire exposed bridge girders, Journal of Constructional Steel Research. 88 (2013) 34–42. https://doi.org/10.1016/j.jcsr.2013.04.007.

[14] S.E. Quiel, Z. Zhu, Numerical Evaluation of a Sample Steel Girder Bridge for a Construction Trailer Fire Underneath (ATLSS Report No. 18-03), Advanced Technology for Large Structural Systems (ATLSS) Engineering Research Center, Bethlehem, PA, 2019. http://rgdoi.net/10.13140/RG.2.2.33593.52321/1 (accessed May 22, 2020).

[15] Z. Zhu, S.E. Quiel, N.E. Khorasani, Bivariate structural-fire fragility curves for simple-span overpass bridges with composite steel plate girders, Structural Safety. 100 (2023) 102294. https://doi.org/10.1016/j.strusafe.2022.102294.

[16] X. Wu, T. Huang, F.T.K. Au, J. Li, Posttensioned Concrete Bridge Beams Exposed to Hydrocarbon Fire, J. Struct. Eng. 146 (2020) 04020210. https://doi.org/10.1061/(ASCE)ST.1943-541X.0002791.

[17] Z. Liu, H. Xie, B. Han, P. Li, Z. Jiang, J. Yu, Experimental study on residual bearing capacity of full-size fire-damaged prestressed concrete girders, Structures. 45 (2022) 1788–1802. https://doi.org/10.1016/j.istruc.2022.10.026.

[18] W. Hou, G. Zhang, S. He, Fire Resistance Tests on Prestressed Concrete Box Girder with Intumescent Fire-Retardant Coatings, Fire Technol. 58 (2022) 107–131. https://doi.org/10.1007/s10694-021-01145-7.

[19] C. Song, G. Zhang, W. Hou, S. He, Performance of prestressed concrete box bridge girders under hydrocarbon fire exposure, Advances in Structural Engineering. 23 (2020) 1521–1533. https://doi.org/10.1177/1369433219898102.

[20] V. Kodur, N.R. Hatinger, A performance-based approach for evaluating fire resistance of prestressed concrete double T-beams, Journal of Fire Protection Engineering. 21 (2011) 185–222. https://doi.org/10.1177/1042391511417795.

[21] M.B. Dwaikat, V.K.R. Kodur, A numerical approach for modeling the fire induced restraint effects in reinforced concrete beams, Fire Safety Journal. 43 (2008) 291–307. https://doi.org/10.1016/j.firesaf.2007.08.003.

[22] Wikipedia, Interstate 85 bridge collapse, (n.d.). https://en.wikipedia.org/wiki/Interstate_85_bridge_collapse (accessed April 19, 2023).

[23] B. Jansen, Atlanta bridge collapse shows how fire defeats concrete, steel, USA Today. (n.d.). https://www.usatoday.com/story/news/2017/03/31/atlanta-bridge-collapse-shows-how-fire-defeats-concrete-steel/99877148/ (accessed April 18, 2019).
[24] ASTM International, ASTM A416-17 Standard Specification for Low-Relaxation, Seven-Wire Steel Strand for Prestressed Concrete, 2017. https://doi.org/10.1520/A0416.
[25] ASTM International, ASTM A615-16 Standard Specification for Deformed and Plain Carbon-Steel Bars for Concrete Reinforcement, 2016. https://doi.org/10.1520/A0615.
[26] M.J. Hurley, D. Gottuk, J.R. Hall, K. Harada, E. Kuligowski, M. Puchovsky, J. Torero, J.M. Watts, C. Wieczorek, eds., SFPE Handbook of Fire Protection Engineering, Springer New York, New York, NY, 2016. https://doi.org/10.1007/978-1-4939-2565-0.
[27] G. Heskestad, Luminous heights of turbulent diffusion flames, Fire Safety Journal. 5 (1983) 103–108. https://doi.org/10.1016/0379-7112(83)90002-4.
[28] CEN, Eurocode 1: Actions on structures -Part 1-5: General actions - Actions on structures exposed to fire, European Committee for Standardization, Brussels, Belgium, 2002. https://doi.org/ICS 91.010.30; 93.040.
[29] J.-M. Franssen, T. Gernay, Modeling structures in fire with SAFIR ®: theoretical background and capabilities, Journal of Structural Fire Engineering. 8 (2017) 300–323.
[30] G.W. Shorter, T.Z. Harmathy, Discussion on the fire resistance of prestressed concrete beams, Proceedings of the Institution of Civil Engineers. 20 (1961) 313–315.
[31] T.Z. Harmathy, Effect of Moisture on the Fire Endurance of Building Elements, ASTM STP 385. American Society for Testing and Materials-Special Technical Publication No. 385 (1965) 74–95. https://doi.org/978-0-8031-5970-9.
[32] V. Zhukov, Reasons of Explosive Spalling of Concrete by Fire, Beton Zhelezobeton (Concrete and Reinforcement Concrete). (1976) 26–28.
[33] Z.P. Bazant, J. Chern, W. Thonguthai, FINITE ELEMENT PROGRAM FOR MOISTURE AND HEAT TRANSFER IN HEATED CONCRETE, Nuclear Engineering and Design. 68 (1981) 61–70. https://doi.org/10.1016/0029-5493(82)90040-1.
[34] G. Choe, G. Kim, M. Yoon, E. Hwang, J. Nam, N. Guncunski, Effect of moisture migration and water vapor pressure build-up with the heating rate on concrete spalling type, Cement and Concrete Research. 116 (2019) 1–10. https://doi.org/10.1016/j.cemconres.2018.10.021.
[35] K.D. Hertz, L.S. Sørensen, Test method for spalling of fire exposed concrete, Fire Safety Journal. 40 (2005) 466–476. https://doi.org/10.1016/j.firesaf.2005.04.001.
[36] L.T. Phan, J.R. Lawson, F.L. Davis, Effects of elevated temperature exposure on heating characteristics, spalling, and residual properties of high performance concrete, Materials and Structures. 34 (2001).
[37] P. Kalifa, G. Chéné, C. Gallé, High-temperature behaviour of HPC with polypropylene fibres: From spalling to microstructure, Cement and Concrete Research. 31 (2001) 1487–1499. https://doi.org/10.1016/S0008-8846(01)00596-8.
[38] P.C. Tatnall, Shotcrete in Fires: Effects of Fibers on Explosive Spalling, Shotcrete. (2002) 10–12.
[39] R. Jansson, L. Boström, The Influence of Pressure in the Pore System on Fire Spalling of Concrete, Fire Technology. 46 (2010) 217–230. https://doi.org/10.1007/s10694-009-0093-9.
[40] F. Wang, M. Wang, J. Huo, The effects of the passive fire protection layer on the behavior of concrete tunnel linings: A field fire testing study, Tunnelling and Underground Space Technology. 69 (2017) 162–170. https://doi.org/10.1016/j.tust.2017.06.021.
[41] Z. Yan, Y. Shen, H. Zhu, Y. Lu, Experimental study of tunnel segmental joints subjected to elevated temperature, Tunnelling and Underground Space Technology. 53 (2016) 46–60. https://doi.org/10.1016/j.tust.2016.01.005.
[42] N. Hua, A. Tessari, N. Elhami Khorasani, Characterizing damage to a concrete liner during a tunnel fire, Tunnelling and Underground Space Technology. 109 (2021) 103761. https://doi.org/10.1016/j.tust.2020.103761.
[43] European Committee for Standardization, Eurocode 2: Design of Concrete Structures - Part 1-2: General Rules - Structural Fire Design, 2004.
[44] K.D. Hertz, Limits of spalling of fire-exposed concrete, Fire Safety Journal. 38 (2003) 103–116. https://doi.org/10.1016/S0379-7112(02)00051-6.
[45] Z.P. Bažant, W. Thonguthai, Pore pressure in heated concrete walls: theoretical prediction, Magazine of Concrete Research. 31 (1979) 67–76. https://doi.org/10.1680/macr.1979.31.107.67.
[46] C.E. Majorana, V. Salomoni, B.A. Schrefler, Hygrothermal and mechanical model of concrete at high temperature, Materials and Structures. 31 (1998) 378–386. https://doi.org/10.1007/BF02480710.
[47] Y. Ichikawa, G.L. England, Prediction of moisture migration and pore pressure build-up in concrete at high temperatures, Nuclear Engineering and Design. 228 (2004) 245–259. https://doi.org/10.1016/j.nucengdes.2003.06.011.

[48] R. Tenchev, P. Purnell, An application of a damage constitutive model to concrete at high temperature and prediction of spalling, International Journal of Solids and Structures. 42 (2005) 6550–6565. https://doi.org/10.1016/j.ijsolstr.2005.06.016.
[49] D. Gawin, F. Pesavento, B.A. Schrefler, Towards prediction of the thermal spalling risk through a multi-phase porous media model of concrete, Computer Methods in Applied Mechanics and Engineering. 195 (2006) 5707–5729.
[50] M.B. Dwaikat, V.K.R. Kodur, Hydrothermal model for predicting fire-induced spalling in concrete structural systems, Fire Safety Journal. 44 (2009) 425–434. https://doi.org/10.1016/j.firesaf.2008.09.001.
[51] M. Li, Z. Wu, H. Kao, C. Qian, W. Sun, Calculation and analysis of pore vapor pressure of concrete exposed to fire, Int. J. Phys. Sci. 5 (2010) 1315–1323.
[52] C.T. Davie, C.J. Pearce, N. Bićanić, Aspects of Permeability in Modelling of Concrete Exposed to High Temperatures, Transp Porous Med. 95 (2012) 627–646. https://doi.org/10.1007/s11242-012-0066-1.
[53] V.K.R. Kodur, S. Banerji, Modeling the fire-induced spalling in concrete structures incorporating hydro-thermo-mechanical stresses, Cement And Concrete Composites. 117 (2021). https://doi.org/10.1016/j.cemconcomp.2020.103902.
[54] F. Lu, Doctoral thesis: On the prediction of concrete spalling under fire, ETH Zurich, 2015. https://doi.org/10.3929/ethz-a-010581905.
[55] M.Z. Naser, Observational Analysis of Fire-Induced Spalling of Concrete through Ensemble Machine Learning and Surrogate Modeling, J. Mater. Civ. Eng. 33 (2021) 04020428. https://doi.org/10.1061/(ASCE)MT.1943-5533.0003525.
[56] J.-C. Liu, Z. Zhang, A machine learning approach to predict explosive spalling of heated concrete, Archiv.Civ.Mech.Eng. 20 (2020) 1–25. https://doi.org/10.1007/s43452-020-00135-w.
[57] K.J. LaMalva, ed., Manual of Practice 138: Structural Fire Engineering, American Society of Civil Engineers, Reston, Virginia, 2018.
[58] CEN, EN 1992-1-2:2004 Eurocode 2: Design of concrete structures - Part 1-2: General rules - Structural fire design, European Commission for Standardization, Brussels, Belgium, 2008.
[59] GID simulation, GiD 13.0.4, (2018). https://www.gidsimulation.com/news-and-events/new-gid-13-1-10d-gid-13-0-4/.
[60] CEN, EN 1993-1-2:2005 Eurocode 3: Design of steel structures - Part 1-2: General rules - Structural fire design, European Committee for Standardization, Brussels, Belgium, 2005.
[61] A.H. Buchanan, Structural Design for Fire Safety, John Wiley & Sons, Chichester, UK., 2001.
[62] AISC, Specification for Structural Steel Buildings (AISC 360-16), American Institute of Steel Construction, Chicago, IL, 2016.
[63] ACI Committee 216, Code Requirements for Determining Fire Resistance of Concrete and Masonry Construction Assemblies, American Concrete Institute, Farmington Hills, MI, 2014.
[64] E. T. T. Lie, Structural Fire Protection., American Society of Civil Engineers, 1992. https://doi.org/10.1002/fam.810040102.
[65] J.-M. Franssen, T. Gernay, User's manual for SAFIR 2019 a computer program for analysis of structures subjected to fire, University of Liege, Liege, Belgium, 2019.
[66] T. Gernay, J.-M. Franssen, A formulation of the Eurocode 2 concrete model at elevated temperature that includes an explicit term for transient creep, Fire Safety Journal. 51 (2012) 1–9. https://doi.org/10.1016/j.firesaf.2012.02.001.
[67] J.H. Kent, A quantitative relationship between soot yield and smoke point measurements, Combustion and Flame. 63 (1986) 349–358. https://doi.org/10.1016/0010-2180(86)90004-0.
[68] M. Muñoz, J. Arnaldos, J. Casal, E. Planas, Analysis of the geometric and radiative characteristics of hydrocarbon pool fires, Combustion and Flame. 139 (2004) 263–277. https://doi.org/10.1016/j.combustflame.2004.09.001.
[69] E. Planas-Cuchi, J.M. Chatris, C. López, J. Arnaldos, Determination of Flame Emissivity in Hydrocarbon Pool Fires Using Infrared Thermography, Fire Technology. 39 (2003) 261–273. https://doi.org/10.1023/A:1024193515227.
[70] V.C. Raj, S.V. Prabhu, Measurement of geometric and radiative properties of heptane pool fires, Fire Safety Journal. 96 (2018) 13–26. https://doi.org/10.1016/j.firesaf.2017.12.003.
[71] S. Sudheer, S.V. Prabhu, Measurement of Flame Emissivity of Hydrocarbon Pool Fires, Fire Technology. 48 (2012) 183–217. https://doi.org/10.1007/s10694-010-0206-5.
[72] S. Sudheer, S.V. Prabhu, Characterization of hexane pool fires using infrared thermography, Journal of Fire Sciences. 31 (2013) 143–165. https://doi.org/10.1177/0734904112459260.
[73] S. Sudheer, S.V. Prabhu, Measurement of flame emissivity of gasoline pool fires, Nuclear Engineering and Design. 240 (2010) 3474–3480. https://doi.org/10.1016/j.nucengdes.2010.04.043.

[74] K. Zhou, N. Liu, L. Zhang, K. Satoh, Thermal Radiation from Fire Whirls: Revised Solid Flame Model, Fire Technology. 50 (2014) 1573–1587. https://doi.org/10.1007/s10694-013-0360-7.
[75] G. Shen, K. Zhou, F. Wu, J. Jiang, Z. Dou, A Model Considering the Flame Volume for Prediction of Thermal Radiation from Pool Fire, Fire Technology. 55 (2019) 129–148. https://doi.org/10.1007/s10694-018-0779-y.
[76] K. Zhou, N. Liu, J.S. Lozano, Y. Shan, B. Yao, K. Satoh, Effect of flow circulation on combustion dynamics of fire whirl, Proceedings of the Combustion Institute. 34 (2013) 2617–2624. https://doi.org/10.1016/j.proci.2012.06.053.
[77] E.E. Zukoski, B.M. Cetegen, T. Kubota, Visible structure of buoyant diffusion flames, Symposium (International) on Combustion. 20 (1985) 361–366. https://doi.org/10.1016/S0082-0784(85)80522-1.
[78] M. Muñoz, E. Planas, F. Ferrero, J. Casal, Predicting the emissive power of hydrocarbon pool fires, Journal of Hazardous Materials. 144 (2007) 725–729. https://doi.org/10.1016/j.jhazmat.2007.01.121.
[79] K.B. McGrattan, H.R. Baum, A. Hamins, NISTIR 6546: Thermal radiation from large pool fires, National Institute of Standards and Technology, Gaithersburg, MD, 2000. https://doi.org/10.6028/NIST.IR.6546.
[80] C.L. Beyler, Chapter 66: Fire Hazard Calculations for Large, Open Hydrocarbon Fires, in: SFPE Handbook of Fire Protection Engineering, 5th Edition, Society of Fire Protection Engineering, New York, NY, 2016: pp. 2591–2663.
[81] D. Drysdale, An Introduction to Fire Dynamics, Third Edition, John Wiley & Sons, Ltd, Chichester, West Sussex, United Kingdom, 2011. https://doi.org/10.1002/9781119975465.
[82] The MathWorks, Inc., MATLAB and Statistics Toolbox, Natick, Massachussetts, 2017.
[83] F. Blondin, P. Blanchet, C. Dagenais, Z. Triantafyllidis, L. Bisby, Fire hazard of compressed straw as an insulation material for wooden structures, Fire and Materials. 44 (2020) 736–746. https://doi.org/10.1002/fam.2851.
[84] W. Song, Y. He, Y. Wu, W. Qu, Characterization of Burning Behaviors and Particulate Matter Emissions of Crop Straws Based on a Cone Calorimeter, Materials. 14 (2021) 3407. https://doi.org/10.3390/ma14123407.
[85] H.A.-H. Ibrahim, Solid Fuel Production from Straw, Recent Advances in Petrochemical Science. 6 (2019). https://doi.org/10.19080/RAPSCI.2019.06.555691.
[86] J.W. Regan, Heat Release Rate Characterization of NFPA 1403 Compliant Training Fuels, Fire Technol. 57 (2021) 1847–1867. https://doi.org/10.1007/s10694-021-01092-3.
[87] A.H. Buchanan, A.K. Abu, Structural Design for Fire Safety, Second edition, John Wiley & Sons Inc, Chichester, West Sussex, United Kingdom, 2017.
[88] H. Ingason, Design fire curves for tunnels, Fire Safety Journal. 44 (2009) 259–265. https://doi.org/10.1016/j.firesaf.2008.06.009.
[89] Q. Guo, S.E. Quiel, C.J. Naito, Traffic-based quantitative risk analysis of structural fire damage to roadway tunnel linings, Structure and Infrastructure Engineering. (2021) 1–17. https://doi.org/10.1080/15732479.2021.1993936.